Solar model uncertainties, MSW analysis, and future solar neutrino experiments

Naoya Hata and Paul Langacker

Department of Physics, University of Pennsylvania, Philadelphia, Pennsylvania 19104

(Received 3 November 1993)

Various theoretical uncertainties in the standard solar model and in the Mikheyev-Smirnov-Wolfenstein (MSW) analysis are discussed. It is shown that two methods give consistent estimations of the solar neutrino flux uncertainties: (a) a simple parametrization of the uncertainties using the core temperature and the nuclear production cross sections; (b) the Monte Carlo method of Bahcall and Ulrich. In the MSW analysis, we emphasize proper treatments of correlations of theoretical uncertainties between flux components and between different detectors, the Earth effect, and multiple solutions in a combined χ^2 procedure. In particular the large-angle solution of the combined observation is allowed at 95% C.L. only when the theoretical uncertainties are included. If their correlations were ignored, the region would be overestimated. The MSW solutions for various standard and nonstandard solar models are also shown. The MSW predictions of the global solutions for the future solar neutrino experiments are given, emphasizing the measurement of the energy spectrum and the day-night effect in Sudbury Neutrino Observatory and Super-Kamiokande to distinguish the two solutions.

I. INTRODUCTION

The solar neutrino experiments of Homestake (chlorine) [1,2], Kamiokande [3,4], and the gallium experiments of SAGE [5,6] and GALLEX [7] show deficits of the neutrino flux from the Sun when compared to the standard solar model (SSM) predictions [8,9] as summarized in Table I. Numerous theoretical proposals have been made to resolve the discrepancy between theory and experiment. Astrophysical solutions in general are, however, strongly disfavored by the data [10,11,7,12–16]. A recent model-independent analysis [16] concluded that, since astrophysical processes cannot significantly distort the neutrino energy spectrum [17], the lower observed Homestake rate relative to the Kamiokande rate excludes essentially all astrophysical explanations. Even with the Homestake experimental error tripled, the combined observations are in contradiction with the explicitly constructed nonstandard solar models [16]. On the other hand, among many particle physics solutions, the Mikheyev-Smirnov-Wolfenstein (MSW) mechanism [18] gives an excellent description of the data, and is taken as a strong hint of neutrino mass and mixings [12,19]. (See also [20–26].)

When constraining the parameter space from the experimental data in the MSW analysis, it is necessary to include relevant theoretical uncertainties properly. In the SSM, the theoretical uncertainty in the initial ^{8}B flux quoted by Bahcall and Pinsonneault [8] is 14%, and is comparable to the experimental uncertainties of Homestake (10%) and Kamiokande (14%). In the Turck-Chièze–Lopes SSM [9], the ^{8}B flux uncertainty is 25% and

dominates the experimental uncertainties.[1] The omission of the theoretical uncertainties underestimates the uncertainty of the MSW parameter space constrained from the experiments.

Equally important, but often ignored, are the correlations among the theoretical uncertainties. Especially, a correct treatment of the ^{8}B flux uncertainty is significant since it is the largest among the theoretical uncertainties and also strongly correlated from experiment to experiment. When one considers the combined fit, for example, it is not legitimate to allow a smaller ^{8}B flux for Homestake and a larger ^{8}B flux for Kamiokande. If the correlations were ignored in the MSW two-flavor oscillation analysis, one obtains a larger parameter space in the large-angle solution and even finds a third allowed region around $\Delta m^2 \sim 10^{-7} \, \mathrm{eV}^2$ and $\sin^2 2\theta \sim 0.7$ at 90% C.L.[2] Moreover, the uncertainties are also correlated among different flux components. For instance, if the opacity were lower than the standard value (or equivalently the core temperature were lower), both the ^{7}Be and ^{8}B fluxes would be reduced. Since the MSW mechanism

---

[1] We use 1σ errors for the Bahcall-Pinsonneault SSM by dividing their quoted 3σ errors by three. The uncertainties estimated in Turck-Chièze–Lopes model are not statistically well-defined quantities, but combined numbers of the measurement errors and the most probable errors [9].

[2] Krauss *et al.* found a third allowed region around $\Delta m^2 \sim 10^{-7} \, \mathrm{eV}^2$ and $\sin^2 2\theta \sim 0.7$ at 90% C.L., but this is due to the omission of the correlations and also the use of old experimental input [24]. Also the uncertainties used in [24] are larger than the estimation of Bahcall and Pinsonneault [8].

TABLE I. The standard solar model predictions of Bahcall and Pinsonneault [8] (BP SSM) and of Turck-Chièze and Lopes [9] (TCL SSM). The Bahcall-Pinsonneault model includes the particle diffusion effect for the first time in the SSM calculation. Also listed are the results of the solar neutrino experiments. The gallium experiment is the combined result of SAGE and GALLEX I and II.

	BP SSM	TCL SSM	Experiments
Kamiokande[a]	1 ± 0.14	0.77 ± 0.19	0.51 ± 0.07 BP SSM
Homestake[b] (SNU)	8 ± 1	6.4 ± 1.4	2.32 ± 0.23 (0.29 ± 0.03 BP SSM)
SAGE[c] & GALLEX[d] (SNU)	$131.5 \, ^{+7}_{-6}$	122.5 ± 7	81 ± 13 (0.62 ± 0.10 BP SSM)

[a]The result of the combined data of 1040 days of Kamiokande II [0.47 ± 0.05 (stat) ± 0.06 (syst) BP SSM] and 514.5 days of Kamiokande III [0.57 ± 0.06 (stat) ± 0.06 (syst) BP SSM] [4].
[b]The result of run 18 to 124 (through May 1993) [2].
[c]The preliminary result of SAGE I (from January 1990 through May 1992) is 70 ± 19 (stat) ± 10 (syst) SNU [6].
[d]The combined result of GALLEX I and II (including 21 runs through April 1993) is 87 ± 14 (stat) ± 7 (syst) SNU [7].

often affects each neutrino flux component differently according to the neutrino energy, the flux uncertainties and their correlations affect nontrivially the allowed parameter space of the combined observations.

Two methods have been proposed to incorporate the flux uncertainties in the MSW analysis. The first method utilizes the Monte Carlo SSM's constructed with randomly chosen input parameters distributed around the mean values [27,28]. Those 1000 SSM's were incorporated in the MSW analysis of Bahcall and Haxton [20], and, recently, of Shi, Schramm, and Bahcall [21]. Krauss, Gates, and White calculated 100 000 Monte Carlo fluxes from the power-law dependence obtained by Bahcall and Ulrich, generating randomly the SSM input parameters with Gaussian distributions, but ignored the uncertainty correlations for different flux components and different experiments [24].

The second method, which we have used in our previous analysis [12,19], parametrizes the SSM flux uncertainties with the central temperature and nuclear reaction cross sections, distinguishing the flux uncertainties due to purely astrophysical effects, such as the uncertainties from the heavy element abundance and other uncertainties in the opacity, from those due to the nuclear cross sections. The astrophysical uncertainties are parametrized by the uncertainty of the central temperature ΔT_C, which is chosen to reproduce the uncertainty of the ^{7}Be flux. This ΔT_C correctly reproduces the uncertainties of the other major fluxes (pp and ^{8}B), and also is consistent with the variation of T_C shown in the plots of the Bahcall-Ulrich Monte Carlo SSM [29]. This scheme, describing the flux uncertainties and their correlations with ΔT_C and the cross-section uncertainties, is calibrated by the 1000 Monte Carlo Bahcall-Ulrich fluxes, and relies on the assumption that those uncertainties are normally distributed, which is true for the Bahcall-Ulrich model. This simple parametrization is useful since it can easily be generalized to other SSM's just by changing those parameters. (On the other hand the Monte Carlo fluxes are not necessarily calculated for every SSM. For example, the Monte Carlo fluxes are not yet available for the latest SSM by Bahcall and Pinsonneault, which uses the most updated input parameters and incorporates

the helium diffusion effect for the first time in the SSM calculation.[3]) Also the parametrization method gives a simple physical picture of the flux uncertainties, and can be generalized to the nonstandard solar models that are in most cases characterized by a lower T_C. We found that the parametrization method reproduces the Bahcall-Ulrich Monte Carlo uncertainties with a surprising accuracy that is sufficient in the solar neutrino analysis.

This parametrization of the uncertainties, however, was questioned on the grounds that such a simplification can lead to errors in describing the nonlinear relations among the neutrino fluxes, which are the output of solving the coupled partial differential equations of stellar structure with nontrivial matching conditions [30,10]. It was argued that a Monte Carlo study is necessary to estimate the uncertainties reliably. Later we will show numerically that, in fact, the uncertainties obtained by the parametrization method are essentially identical to the Monte Carlo results.

In this paper we discuss various technical but important issues concerning the theoretical uncertainties in the solar neutrino data analysis. In Sec. II we show that the parametrization method reproduces the SSM uncertainties obtained by the Monte Carlo method. The comparison is made for both the uncertainties of flux components and their correlations. We also compare the two methods for the uncertainties and their correlations of the predicted rates for different solar neutrino detectors.

Once the equivalence of the two methods is established for the SSM we compare them in the MSW analysis in Sec. III. The allowed regions calculated by both meth-

---

[3]One could construct the Monte Carlo SSM's for the Bahcall-Pinsonneault model by (a) using the 1000 Bahcall-Ulrich fluxes by rescaling the central values and their uncertainties to the Bahcall and Pinsonneault model or (b) creating one's own Monte Carlo fluxes by using the power laws of Bahcall and Ulrich with the updated input parameters. Since these do not include the effect of the particle diffusion, there is no guarantee that those methods provide more accurate estimation of the flux uncertainties than the parametrization method.

ods are shown. The effect of the theoretical uncertainties and their correlations are displayed for the global MSW analysis. Other theoretical issues are also considered in Sec. III. Analytic approximations for the MSW transitions by Petcov, Parke, and Pizzochero are compared and the associated uncertainties are discussed. Another issue involves the estimate of confidence level (C.L.) in the presence of multiple fit solutions. We emphasize that there are several possible definitions of the C.L. contours, leading to slightly different allowed regions, and give a statistical definition of the C.L. contours of the most conservative (and we believe the best) prescription. We also compare the allowed MSW parameter space for the SSM

with increased uncertainties and the SSMs of different authors.

We conclude Sec. III by presenting the current results of our MSW fits for transitions into both ordinary (ν_μ, ν_τ) and sterile neutrinos, incorporating the theoretical issues and uncertainties discussed above. These also include the regeneration in the Earth (Earth effect), which is important for some regions of the MSW parameters for both time-averaged data and day-night asymmetries [31,19]. We find that the data is fit extremely well by the MSW effect for transitions into ordinary neutrinos for $\Delta m^2 \sim 6 \times 10^{-6}$ eV^2 and $\sin^2 2\theta \sim 7 \times 10^{-3}$ (the nonadiabatic) solution, although there is a second (large-angle)
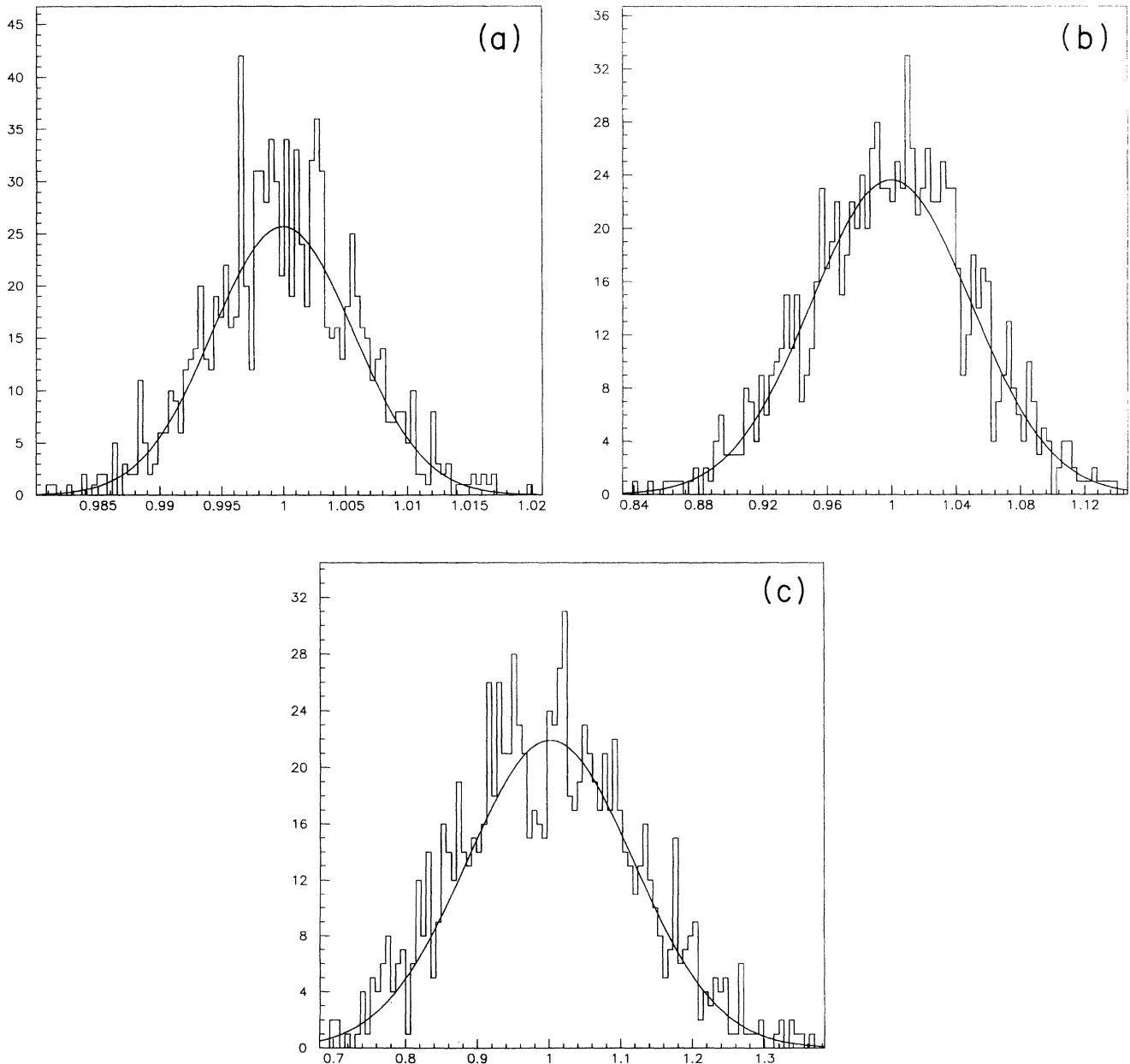
FIG. 1. The distributions of the (a) pp, (b) ^{7}Be, and (c) ^{8}B flux of the 1000 Monte Carlo SSM's by Bahcall-Ulrich (histograms) are fit with the parametrized method (solid curves) that assumes Gaussian distributions of the central temperatures and the nuclear reaction cross sections around their central values.

solution with $\Delta m^2 \sim 9 \times 10^{-6}\,\mathrm{eV}^2$ and $\sin^2 2\theta \sim 0.6$ which is marginally allowed at 90% C.L. There is also a poorer but acceptable fit for transitions into sterile neutrinos in the nonadiabatic region.

The MSW effect can be also considered in the nonstandard solar models, and the combined fits to explicitly constructed nonstandard solar models are shown in Sec. IV. The results of the MSW fit using the core temperature and the ^{8}B flux each as a free parameter are

displayed. In Sec. V, the prospects for the future solar neutrino experiments are considered. We discuss in detail the predictions for the energy spectrum measurement and the Earth effect in Sudbury Neutrino Observatory (SNO) and Super-Kamiokande to distinguish the two solutions obtained from the global analysis: a spectrum distortion is predicted for the nonadiabatic solution, while a characteristic day-night effect is expected for the large-angle solution.
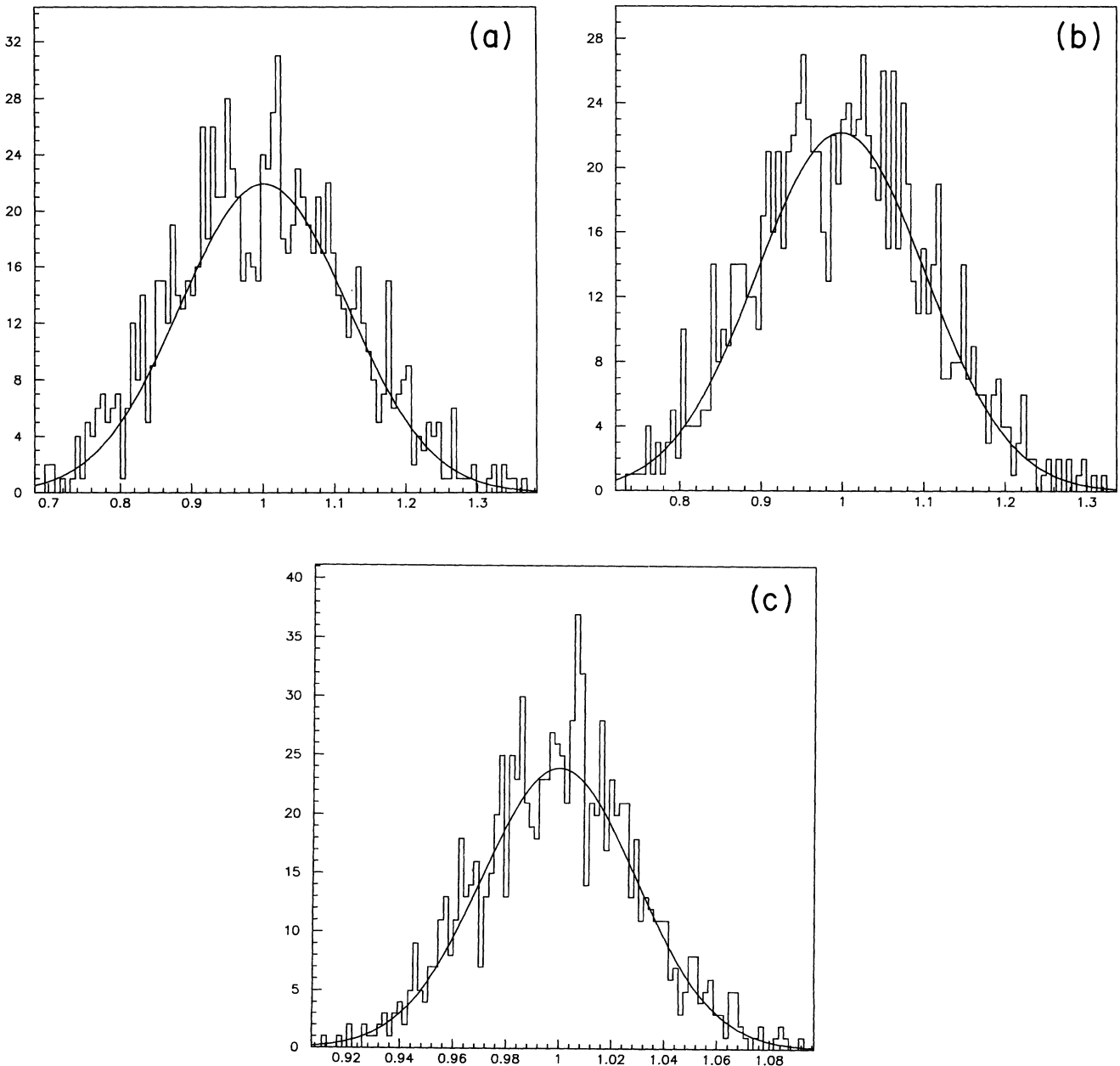
FIG. 2. The distributions of the experimental rates obtained from Bahcall-Ulrich Monte Carlo fluxes for the (a) Kamiokande, (b) chlorine, and (c) gallium experiments (histograms). They are compared with the rate distributions obtained from the parametrized fluxes (solid curve). In both cases the detector cross-section uncertainties are not included.

II. COMPARISON OF THE PARAMETRIZED UNCERTAINTIES AND THE MONTE CARLO RESULTS

A. The flux uncertainties

In our parametrization method [12,19], the basic assumption is that the SSM flux uncertainties are expressed by a few parameters that have physical meanings, and that those uncertainties are approximated by Gaussian distributions. If the flux uncertainties and their correlations are found non-Gaussian by the Monte Carlo estimation, our parametrization method cannot be used. First we studied the distributions of the 1000 Monte Carlo SSM fluxes calculated by Bahcall and Ulrich with randomly chosen input parameters [27,28], and confirmed that they indeed have Gaussian distributions. In Fig. 1, the histograms are the distribution of the Monte Carlo fluxes of the pp, ^{7}Be, and ^{8}B neutrinos; the solid lines are our fit with the Gaussian form. The rate predictions for solar neutrino detectors were also studied and are displayed in Fig. 2, which are also fit with the Gaussian form. In both cases, the fits are excellent.

Second, we utilize the observation that the neutrino fluxes are well described by a power law in the central temperature [29]:

$$\phi(pp) \sim T_C^{-1.2}, \quad \phi(\mathrm{Be}) \sim T_C^8, \quad \text{and } \phi(\mathrm{B}) \sim T_C^{18}, \quad (1)$$

where our units are such that $T_C = 1 = 15.67 \times 10^6$ K for the central value of the SSM. We express the astrophysical uncertainties of the major fluxes (pp, ^{7}Be, and ^{8}B) with the uncertainty of the central temperature times the exponent in the power law. We identify the main sources of the astrophysical uncertainties as the heavy element abundance and other uncertainties in the opacity. The other uncertainties, independent of such astrophysical effects, are from the nuclear reaction cross sections, especially for the cross sections of $p+^7$Be and ^{3}He$+^4$He. Those cross sections are expressed by S factors S_{17} and S_{34}, respectively.[4] Our choice of the relevant cross sections is based on the fact that the ^{8}B flux is directly proportional to S_{17}, and the ^{7}Be and ^{8}B fluxes are proportional to S_{34} [32]. The flux uncertainties and their correlations are ex-

TABLE II. The parameters of the SSM flux uncertainties. n is the exponent in the T_C power law, and $s_k = \Delta S_k/S_k$ ($k = 34, 17$) are the fractional flux uncertainties due to the nuclear reaction cross section ^{3}He$+^4$He and $p+^7$Be. We quote s_k from Refs. [27,8]. We determine ΔT_C to be 0.0057 for Bahcall-Ulrich SSM and 0.0060 for the Bahcall-Pinsonneault SSM.

	n	s_{34}	s_{17}
Bahcall-Ulrich SSM ($\Delta T_C = 0.0057$)			
pp	-1.2	0	0
^{7}Be	8	0.02	0
^{8}B	18	0.02	0.07
Bahcall-Pinsonneault SSM ($\Delta T_C = 0.0060$)			
pp	-1.2	0	0
^{7}Be	8	0.032	0
^{8}B	18	0.032	0.093

pressed by those three parameters[5] (ΔT_C, $\Delta S_{17}/S_{17}$, and $\Delta S_{34}/S_{34}$). Their contribution to each flux is displayed in Table II. The magnitude of the uncertainties of the major fluxes[6] are the quadrature sum of those uncertainties:

$$\frac{\Delta \phi^i}{\phi^i} = \left[(n_i \Delta T_C)^2 + \sum_{k=34,17} (s_k^i)^2 \right]^{1/2}, \quad (2)$$

where $i = pp, ^7\mathrm{Be}, ^8\mathrm{B}$. n_i are the temperature exponents ($\phi^i \sim T_C^{n_i}$), and s_k^i are the fractional uncertainty in ϕ^i from $\Delta S_{17}/S_{17}$ and $\Delta S_{34}/S_{34}$ listed in Table II for both the Bahcall-Ulrich and Bahcall-Pinsonneault model. ΔT_C is not explicitly given in the SSM calculation. We determine ΔT_C so that the uncertainties defined above correctly reproduce the ^{7}Be flux uncertainty given in the Bahcall-Ulrich or Bahcall-Pinsonneault SSM. We obtained $\Delta T_C = 0.0057$ for the Bahcall-Ulrich model, and $\Delta T_C = 0.0060$ for the Bahcall-Pinsonneault model. The resulting ΔT_C is consistent with the flux uncertainties of pp and ^{8}B assigned in those models. For the Bahcall-Ulrich SSM this choice of ΔT_C is also consistent with the T_C distribution plotted for the Monte Carlo SSM's [29]. The Monte Carlo SSM's of the Bahcall-

---

[4]While the $p+^7$Be cross section has little effect on solar conditions other than the ^{8}B flux, other cross sections such as $p + p$ (S_{11}) and ^{3}He$+^3$He (S_{33}) directly affect the energy generation and cannot be separated from the astrophysical uncertainties. In particular, the $p + p$ reaction is the main source of the energy production, and a change of S_{11} leads to a change in T_C. We therefore consider that the effects of the uncertainties in S_{11} and S_{33} are included in ΔT_C.

[5]We could extend this parametrization method by taking into account all nine SSM input parameters using the partial derivatives of the neutrino fluxes obtained from the Monte Carlo SSM's [32]. This should completely reproduce the Monte Carlo results. We will show, however, that our minimal choice of the parameters is sufficient to describe the SSM uncertainties.

[6]We similarly parametrized the minor fluxes [^{13}N, ^{15}O, ^{17}F, $p + e + p$ (pep), and ^{3}He $+ p$ (hep)] using T_C exponents $n = 22, 28.5, 28.8, 2.8$, and 4.5, respectively, and reproduce the amplitude of the uncertainties. However, the T_C exponents for these fluxes except hep are not obtained in Refs. [27,28], and we do not reproduce the correlations of the pep and hep neutrinos with others properly. In the MSW calculations, the effect of the correlations among the minor fluxes is completely negligible.
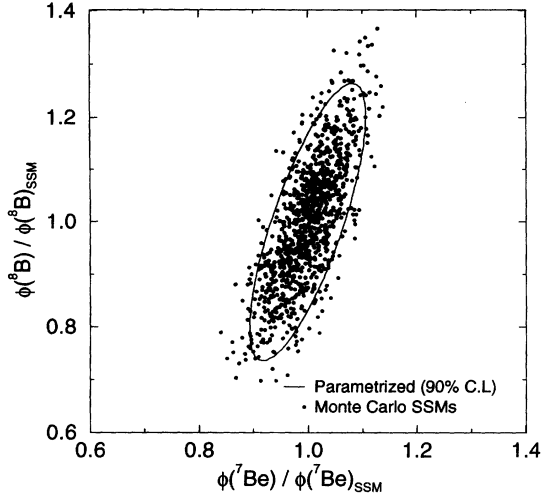
FIG. 3. The distributions of the ^{7}Be and ^{8}B flux of the Bahcall-Ulrich SSM's (dots), and the 90% C.L. contour of our parametrized SSM (solid curve). The magnitudes and the correlations of the fluxes are in excellent agreement for the two methods.

Pinsonneault model are not yet available.

The correlation matrix of the flux uncertainties is given by

$$C_{ij} = \left(n_i n_j (\Delta T_C)^2 + \sum_{k=34,17} s_k^i s_k^j \right) \Big/ \left(\frac{\Delta \phi^i}{\phi^i} \frac{\Delta \phi^j}{\phi^j} \right),$$

(3)

where $i, j = pp, ^7\text{Be}, ^8\text{B}$.

The result of those uncertainties are compared to the Bahcall-Ulrich Monte Carlo SSM's, whose flux uncertainties are calculated by

$$\frac{\Delta \phi^i}{\phi^i} = \left[\frac{1}{N} \sum_{m=1}^N \left(\frac{\phi_m^i}{\phi^i} - 1 \right)^2 \right]^{1/2},$$

(4)

where ϕ_m^i are the ith fluxes of the Monte Carlo SSM's $(m = 1, \dots, N = 1000)$; $\phi^i [= (\sum_{m=1}^N \phi_m^i)/N]$ is the mean

TABLE III. The magnitudes of flux uncertainties $(\Delta \phi / \phi$ at $1\sigma)$ quoted from the Bahcall-Ulrich SSM [27], of the Bahcall-Ulrich Monte Carlo SSM's (Gaussian fit), and of the parametrized Bahcall-Ulrich SSM using the central temperature and the nuclear reaction cross sections. Also listed are the uncertainties of the Bahcall-Pinsonneault SSM and of its parametrized fluxes. (The Monte Carlo study of the Bahcall-Pinsonneault model is not available.)

	pp	^{7}Be	^{8}B
Bahcall-Ulrich SSM	0.0059	0.050	0.12
Bahcall-Ulrich SSM (Monte Carlo)	0.0067	0.05	0.17
Parametrized ($\Delta T_C = 0.0057$)	0.0069	0.05	0.13
Bahcall-Pinsonneault SSM	0.0067	0.06	0.14
Parametrized ($\Delta T_C = 0.0060$)	0.007	0.06	0.15

TABLE IV. The correlation matrices of flux uncertainties obtained from the Bahcall-Ulrich Monte Carlo SSM's and the parametrization method. The agreement between the two methods is good, especially for the $pp - ^7$Be element.

	pp	^{8}B	^{7}Be
Bahcall-Ulrich SSM (Monte Carlo)			
pp	1		
^{8}B	−0.73	1	
^{7}Be	−0.92	0.74	1
Parametrized with ΔT_C and Δs			
pp	1		
^{8}B	−0.81	1	
^{7}Be	−0.92	0.80	1

value of the Monte Carlo fluxes. The correlation matrix is obtained by

$$C_{ij} = \frac{1}{N} \sum_{m=1}^N \left(\frac{\phi_m^i}{\phi^i} - 1 \right) \left(\frac{\phi_m^j}{\phi^j} - 1 \right) \Big/ \left(\frac{\Delta \phi^i}{\phi^i} \frac{\Delta \phi^j}{\phi^j} \right).$$

(5)

The results of the two calculations are compared in Table III for the magnitudes of the uncertainties and Table IV for the correlations. The agreement of the magnitudes are excellent. The correlation matrices are also in good agreement especially for the pp-Be element. In Fig. 3, we display the distribution of Monte Carlo fluxes and our parametrization in the $\phi(\text{Be}) - \phi(\text{B})$ plane; the agreement of the two methods are remarkable.

B. The rate uncertainties

The comparison of the two methods is also carried out for the predictions for different solar neutrino detectors. The fraction of contribution f_i^d of the ith flux component to the dth detector $(d =$Kamiokande, Cl, Ga) are listed in Table V. The SSM uncertainty of the rate R^d (in units

TABLE V. The fractional contribution from flux components for the predicted SSM rates for the different solar neutrino detectors. The total SSM value is normalized to one.

	Kamiokande	Cl	Ga
Bahcall-Ulrich SSM			
pp	0	0	0.536
^{7}Be (I)	0	0	0.009
^{7}Be (II)	0	0.139	0.251
^{8}B	1	0.772	0.106
pep	0	0.025	0.023
^{13}N	0	0.013	0.029
^{15}O	0	0.038	0.046
Bahcall-Pinsonneault SSM			
pp	0	0	0.538
^{7}Be (I)	0	0	0.009
^{7}Be (II)	0	0.150	0.264
^{8}B	1	0.775	0.105
pep	0	0.025	0.024
^{13}N	0	0.013	0.023
^{15}O	0	0.038	0.037

TABLE VI. The comparison of the magnitudes of rate uncertainties for the Bahcall-Ulrich SSM, Monte Carlo SSMs, and the parametrized SSM. Also listed are the uncertainties in the Bahcall-Pinsonneault SSM and its parametrized SSM. The detector cross-section uncertainties are included in the chlorine (Cl) and gallium (Ga) uncertainties.

	Kamiokande	Cl	Ga
Bahcall-Ulrich SSM	0.12	0.11	+0.05 − 0.04
Monte Carlo	0.12	0.11	0.05
Parametrized ($\Delta T_C = 0.0057$)	0.13	0.11	0.05
Bahcall-Pinsonneault SSM	0.14	0.13	0.05
Parametrized ($\Delta T_C = 0.0060$)	0.15	0.13	0.05

of the central values of the SSM) for each detector is a quadratic sum of the flux uncertainties and the detector cross-section uncertainties $\Delta\sigma^d/\sigma^d$, which is 0.033 and 0.04 for the Cl and Ga detector, respectively [27,28]:

$$\Delta R^d = \left[\sum_{i=\text{fluxes}} \left(f_i^d \frac{\Delta\phi^i}{\phi^i} \right)^2 + \left(\frac{\Delta\sigma^d}{\sigma^d} \right)^2 \right]^{1/2}. \quad (6)$$

Those uncertainties are correlated by the ΔT_C and s_k^i through the fluxes; the error matrix is

$$V_{cd} = \sum_{i,j=\text{fluxes}} f_i^c f_j^d \left(n^i n^j (\Delta T_C)^2 + \sum_{k=34,17} s_k^i s_k^j \right), \quad (7)$$

where c, d = Kamiokande, Cl, Ga. Here (and below) the correlation matrix D_{cd} is related to the error matrix by

$$D_{cd} = \frac{V_{cd}}{\Delta R^c \Delta R^d}. \quad (8)$$

Among the correlations, the ^{8}B flux uncertainty is most significant because of its large amplitude and strong correlation between the experiments, especially between the Kamiokande and Cl rate.

For the Monte Carlo method, the rate for the mth Monte Carlo SSM for the dth detector is given by

$$R_m^d = \sum_{i=\text{fluxes}} f_i^d \frac{\phi_m^i}{\bar{\phi}^i}. \quad (9)$$

TABLE VII. The comparison of the correlation matrices of rate uncertainties for the Bahcall-Ulrich Monte Carlo SSMs and the parametrized SSM. The agreement is excellent.

	Kamiokande	Cl	Ga
Bahcall-Ulrich SSM (Monte Carlo)			
Kamiokande	1		
Cl	0.997	1	
Ga	0.92	0.95	1
Parametrized with ΔT_C and Δs			
Kamiokande	1		
Cl	0.996	1	
Ga	0.90	0.94	1

The rate uncertainties for the dth detector is

$$\Delta R^d = \left[\frac{1}{N} \sum_{m=1}^{N} (R_m^d - 1)^2 \right]^{1/2}. \quad (10)$$

The error matrix element between the cth and dth detectors is

$$V_{cd} = \frac{1}{N} \sum_{m=1}^{N} (R_m^c - 1)(R_m^d - 1). \quad (11)$$

We compare the uncertainties and their correlations for the rates in Tables VI (magnitudes) and VII (correlations). The parametrization method reproduces the Monte Carlo results with remarkable accuracy.

III. THE THEORETICAL UNCERTAINTIES IN THE MSW ANALYSIS

A. The SSM uncertainties

We incorporate the SSM flux uncertainties described above in the MSW analysis using a χ^2 method. The MSW calculations of the theoretical rate predictions for each experiment are described in Refs. [12,19]. (See also Refs. [33–40].) The MSW rate for the dth detector (d = Kamiokande, Cl, Ga) is

$$R_{\text{MSW}}^d(\sin^2 2\theta, \Delta m^2) = \sum_{i=\text{fluxes}} f_i^d P_i^d(\sin^2 2\theta, \Delta m^2), \quad (12)$$

where P_i^d is the MSW survival probability of the fluxes [i represents nine flux components, pp, ^{7}Be(I), ^{7}Be(II), ^{8}B, ^{13}N, ^{15}O, ^{17}F, pep and hep] after integrating over the neutrino production site and the neutrino energy including the detector cross sections; for Kamiokande the detector resolution and efficiency are also included when integrating over the recoil electron energy. The formula is also valid with the time-averaged Earth effect (but not with the Kamiokande II day-night data with six time bins). We calculate a χ^2 value for each point in the $\sin^2 2\theta - \Delta m^2$ parameter space:

$$\chi^2(\Delta m^2, \sin^2 2\theta) = \sum_{c,d=\text{Kam, Cl, Ga}} (R^c_{\text{expt}} - R^c_{\text{MSW}})\ (V^{-1})_{cd}\ (R^d_{\text{expt}} - R^d_{\text{MSW}}),\qquad(13)$$

where R_{expt} are the experimental values listed in Table I. V is the 3×3 error matrix and its diagonal elements are the quadratic sum of the experimental uncertainties, the detector cross-section uncertainties, and the SSM flux uncertainties:

$$V_{dd} = (\Delta R^d_{\text{expt}})^2 + \left(\frac{\Delta\sigma^d}{\sigma^d} R^d_{\text{MSW}}\right)^2$$
$$+ \sum_{i=\text{fluxes}} \left(P^d_i f^d_i \frac{\Delta\phi^i}{\phi^i}\right)^2.\qquad(14)$$

The off-diagonal elements describe the correlations of the flux uncertainties described by ΔT_C and s^i_k:

$$V_{cd} = \sum_{i,j=\text{fluxes}} P^c_i P^d_j f^c_i f^d_j \left[n^i n^j (\Delta T_C)^2 \right.$$
$$\left. + \sum_{k=34,17} s^i_k s^j_k \right].\qquad(15)$$

For the Monte Carlo SSMs, the χ^2 is defined by a Monte Carlo average of the probability function:

$$\exp(-\chi^2/2) = \frac{1}{N} \sum_{m=1}^{N} \exp(-\chi^2_m/2),\qquad(16)$$

where χ^2_m is the χ^2 value calculated for the mth Monte Carlo SSM ($m = 1, \ldots, N = 1000$),

$$\chi^2_m = \sum_{d=\text{Kam,Cl,Ga}} \frac{(R^d_{\text{expt}} - R^d_{m,\text{MSW}})^2}{(\Delta R^d_{\text{expt}})^2 + (R^d_{m,\text{MSW}} \Delta\sigma^d/\sigma^d)^2},$$
$$\qquad(17)$$

with the MSW predicted rate for the mth Monte Carlo simulation,

$$R^d_{m,\text{MSW}} = \sum_{i=\text{fluxes}} P^d_i f^d_i \frac{\phi^i_m}{\phi^i}.\qquad(18)$$

We compare[7] the Monte Carlo result and the parametrized method for both the Bahcall-Ulrich model

---

[7]The 95% C.L. allowed regions in Figs. 4–9, 11, 15–20, and 26 are defined by $\chi^2(\sin^2 2\theta, \Delta m^2) \leq \chi^2_{\text{min}} + \Delta\chi^2$ with $\Delta\chi^2 = 6.0$ for both combined fits and individual experiment fits, which corresponds to Gaussian errors in two parameters. Improved definitions for $\Delta\chi^2$ in the combined fits will be discussed later. For the individual experiments we use $\Delta\chi^2 = 6.0$ (2 DF) instead of 3.9 (1 DF), since it is a more conservative estimate of the uncertainties and also easier to compare with the combined fits. (The latter would correspond to mapping a one-parameter confidence region onto a band in a two-parameter space.)

and the Bahcall-Pinsonneault model in Fig. 4 when the Earth effect is ignored. The agreement between the Monte Carlo SSMs and the Bahcall-Ulrich model with our parametrization is excellent.

It is important to include the possibility of ν_e regeneration in the Earth [31,19]. This affects the time-averaged rates and in addition, Kamiokande has searched for a day-night asymmetry by binning their data with respect to the angle between the nadir and the Sun. No asymmetry was observed.

One can easily generalize Eqs. (14) and (15) to include the Kamiokande day-night data point [41] by expanding the error matrix to 9×9, representing the time-averaged rates of Homestake, gallium, Kamiokande III, and the six Kamiokande II day-night data points [19]. We have scaled the normalized Kamiokande II day-night data taken from Ref. [41] to the quoted Kamiokande II average value. Also we have added to each of the six bins the overall systematic uncertainty (15%) from the energy calibration, the angular resolution, and the event selection, which are factored out in the quoted normalized data. (We checked consistency by combining the six bins and reproducing the quoted average Kamiokande II rate.) The systematic uncertainty as well as the SSM flux uncertainties are properly correlated among the six bins and the other uncertainties.

Figure 5 shows the MSW allowed regions for the different uncertainty estimations when the Earth effect is included. Again we conclude that the two methods yield essentially the same results, although the obtained large-angle region is slightly smaller in the parametrization method.

We demonstrate the effect of the theoretical uncertainties by comparing the allowed MSW regions calculated without the flux and detector cross-section uncertainties. Figure 6(a) is the result without the theoretical uncertainties using the Bahcall-Pinsonneault SSM. When compared to Fig. 5(c), the nonadiabatic allowed region is noticeably smaller; there is no large-angle solution at 95% C.L.

The omission of the correlation of uncertainties among the experiments can lead to a overestimation of the allowed parameter space in the large angle solution. To demonstrate the effect of the correlations, we have calculated the allowed regions without the correlations of the theoretical uncertainties between the different experiments [i.e., the off-diagonal elements in the error matrix in Eq. (15) are set to zero]. The result is shown in Fig. 6(b). The correlations are most significant in the large-angle region where the predicted Homestake rate is larger than its experimental central value, while the Kamiokande rate is smaller than its experimental central value, and the ^{8}B flux uncertainty does not enlarge the allowed region if the correlation between the two experiments are properly taken into account. Without the correlations, the allowed parameter space become larger. In Fig. 6(c) we display the allowed region ignoring both the
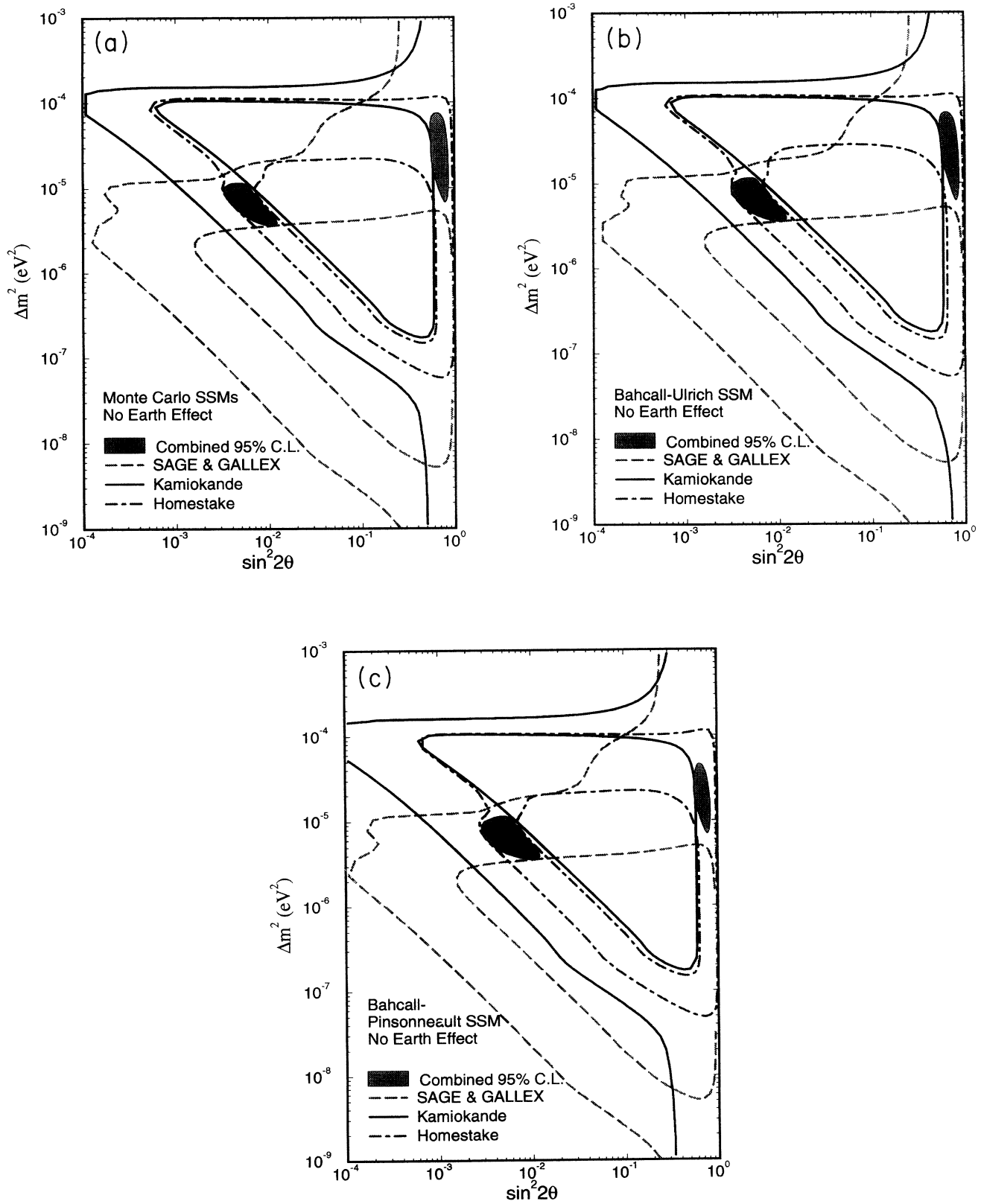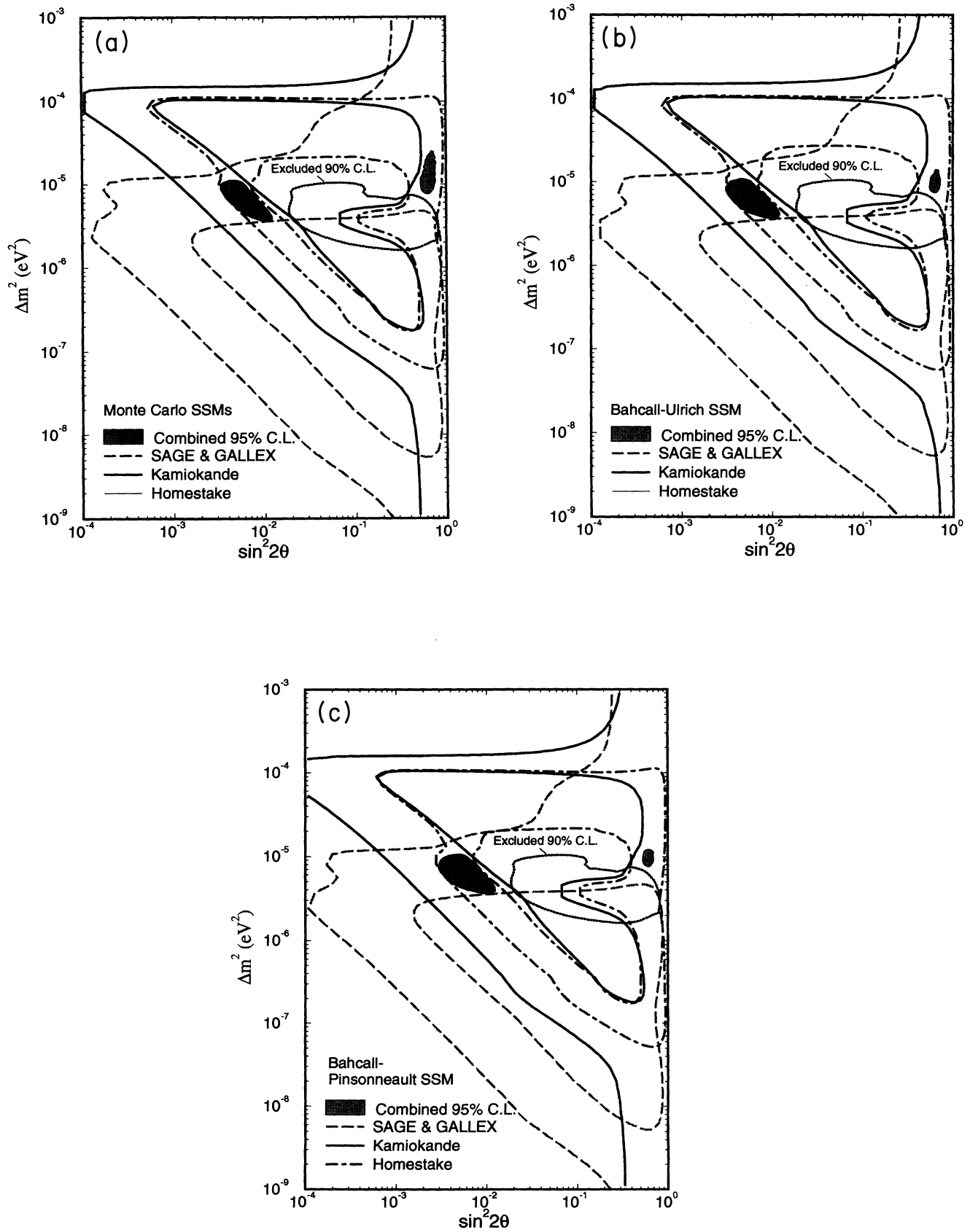
FIG. 4. The allowed regions of the Homestake, Kamiokande, and gallium experiments, and the combined observations. The Earth effect is not included. The SSM uncertainties are calculated by (a) the Bahcall-Ulrich 1000 Monte Carlo SSM's, (b) the parametrized Bahcall-Ulrich SSM, and (c) the parametrized Bahcall-Pinsonneault SSM. The comparison of (a) and (b) shows that the Monte Carlo method and our parametrization method are essentially equivalent. The allowed regions are defined by $\chi^2(\sin^2 2\theta, \Delta m^2) \leq \chi^2_{min} + \Delta\chi^2$ with $\Delta\chi^2 = 6.0$ at 95% C.L.

FIG. 5. Same as Fig. 4, except that the Earth effect is included. The Kamiokande day-night data exclude the region shown with a dotted line (90% C.L.), and are incorporated in the combined fit.

FIG. 6. The experimental constraints on the MSW parameters assuming the Bahcall-Pinsonneault SSM when (a) the theoretical uncertainties of the SSM fluxes and the detector cross sections are ignored, (b) the theoretical uncertainties are included, but their correlations between the fluxes and between the experiments are ignored. Displayed in (c) is the result at 90% C.L. calculated with the same condition in Ref. [24]: the correlations and the Earth effect are ignored and the same experimental input parameters are used. The omission of the correlations overestimates the allowed large-angle regions.

FIG. 7. The experimental constraints when the Turck-Chièze–Lopes SSM is assumed. The two figures are (a) without and (b) with the Earth effect. No constraints are obtained at 95% C.L. from the upper limit of the the Kamiokande result, and the Kamiokande allowed regions are outside the triangles with the solid lines. The region excluded by the Kamiokande II day-night data is shown with the dotted line (90% C.L.) in (b).

FIG. 8. The experimental constraints (a) when theoretical uncertainties of the Bahcall-Pinsonneault SSM fluxes and the detector cross sections are doubled and (b) the Homestake experimental uncertainty is tripled. The Earth effect and the Kamiokande II day-night data are included in both cases.

correlations and the Earth effect, and also using the same experimental values used in Ref. [24]. The large-angle solution stretches to Δm^2 as small as about $10^{-7}\,\mathrm{eV}^2$ even at 90% C.L. Thus, the claim in Ref. [24] that the allowed region is very large was in fact due to their neglect of the correlations.

The allowed parameter space is significantly enlarged if the Turck-Chièze–Lopes SSM is used (Fig. 7), which does not include the particle diffusion effect and predicts the smallest ^{8}B flux and has the largest uncertainties among the recently calculated SSM's [8,9,27,42,43]. The flux uncertainties in this model are not statistical quantities but are the combined numbers of the measurement errors and the most probable errors [9]. Therefore the allowed regions should be taken as qualitative. We display Fig. 7 to illustrate the allowed regions when the fluxes are as low as in the Turck-Chièze–Lopes SSM.

We have also carried out the MSW calculations with doubled theoretical uncertainties [Fig. 8(a)], and with a tripled the Homestake experimental uncertainty [Fig. 8(b)].

The neutrino production distribution in the core and the electron density distributions in the Sun and in the Earth are potential sources of the uncertainties that are not included in the MSW calculations above. The MSW allowed regions were calculated using the electron density distributions and the neutrino production profiles of three different SSMs: the Bahcall-Ulrich SSM and the Bahcall-Pinsonneault SSM with and without the helium diffusion effect. (We used the Bahcall-Pinsonneault flux magnitude for all three calculations.) The combined allowed regions are completely indistinguishable in the three cases. We have also changed those quantities more drastically by varying the peak location of the neutrino production profile in the solar core, the electron density scale height in the entire Sun, and the depth of the core-mantle boundary in the Earth each by $\pm$ 10%, and have repeated the calculations. Again no change was observed in the combined allowed parameter space.

B. Analytic approximations in the MSW calculations

Instead of solving the MSW differential equation numerically,[8] we have calculated the neutrino survival probability with an analytic approximation proposed by Petcov [37] that is obtained from an exact solution of the equation, assuming an exponential form of the electron density distribution in the Sun, which is a good approximation except for inside the core region ($< 0.15 \times R_\odot$, where $R_\odot$ is the solar radius). The Parke formula [33], another approximation that is the simplest and assumes a linear electron density, yields essentially the same MSW plots as Petcov formula except for $\Delta m^2/E \leq 3 \times 10^{-8}\mathrm{eV}^2/\mathrm{MeV}$ [see Fig. 9(b)], where

the density variation is no longer well approximated with a linear function within the neutrino oscillation length. The adiabaticity proposed by Pizzochero assuming the exponential electron density also gives a good approximation except for $\Delta m^2/E \leq 7 \times 10^{-9}\mathrm{eV}^2/\mathrm{MeV}$ [see Fig. 9(c)], where the approximation fails because the oscillation length becomes larger than the density scale height at large angles. The three approximations are compared for the Kamiokande rate in Fig. 9; differences are noticeable in the large angle with small Δm^2.

One limitation of the Petcov formula (as well as the other two) is that it fails to describe nonadiabatic level crossing when the neutrino production point is at or close to the resonant point.[9] As discussed by Krastev and Petcov [23], however, both of the global solutions shown in Fig. 5 are safe from this limitation. For the ^{7}Be and ^{8}B neutrinos with energies relevant for the experiments, the resonance takes place at $\sim 0.15R_\odot$ and $\sim 0.4R_\odot$, respectively, while most of those neutrinos are produced within $0.1R_\odot$. The pp neutrinos are potentially dangerous since their energy corresponds to the resonance at or close to the center of the Sun, and there is a substantial overlap with the production site; however, in the allowed parameter space of the global fit, the MSW transitions of the pp are adiabatic and well described by the Petcov formula. We estimate that the uncertainty for the global fit due to the analytic approximation is $\leq 1\%$.

C. Confidence level definitions

There are differences of the combined allowed MSW regions in the literature. Especially the large-angle regions shown in Refs. [21,23,24] are larger than our calculation, and even a third solution is allowed at 90% C.L. for $\Delta m^2 \sim 10^{-7}\mathrm{eV}^2$ and $\sin^2 2\theta \sim 0.7$. The possible sources of the difference are treatment of the SSM flux uncertainties and their correlations, the treatment of the Earth effect, the MSW analytic approximations, and the experimental input data, some of which have been discussed above. The most significant difference, however, comes from the statistical definition of the confidence levels, rather than the details in MSW calculations.

In the joint χ^2 analysis above, we have used

$$\chi^2(\sin^2 2\theta, \Delta m^2) \leq \chi^2_{\min} + \Delta\chi^2 \qquad (19)$$

with $\Delta\chi^2 = 6.0$ as the 95% confidence level (C.L.) region in the two-dimensional $\log\sin^2 2\theta - \log\Delta m^2$ plane, where $\chi^2_{\min}$ is the global χ^2 minimum. This definition assumes a Gaussian distribution of the probability density around the global minimum, which is only an approximation in our case, particularly when we have multiple χ^2 minima. Another definition used in the literature is to take the combined allowed regions simply as the overlap of the different experiments as shown in Fig. 10. (See also

---

[8]The exact numerical integrations were calculated recently by Fiorentini *et al.* [26]. See the Note added at the end of this paper.

[9]An analytic prescription when the neutrino production site overlaps with the resonance point is discussed by Haxton [35].
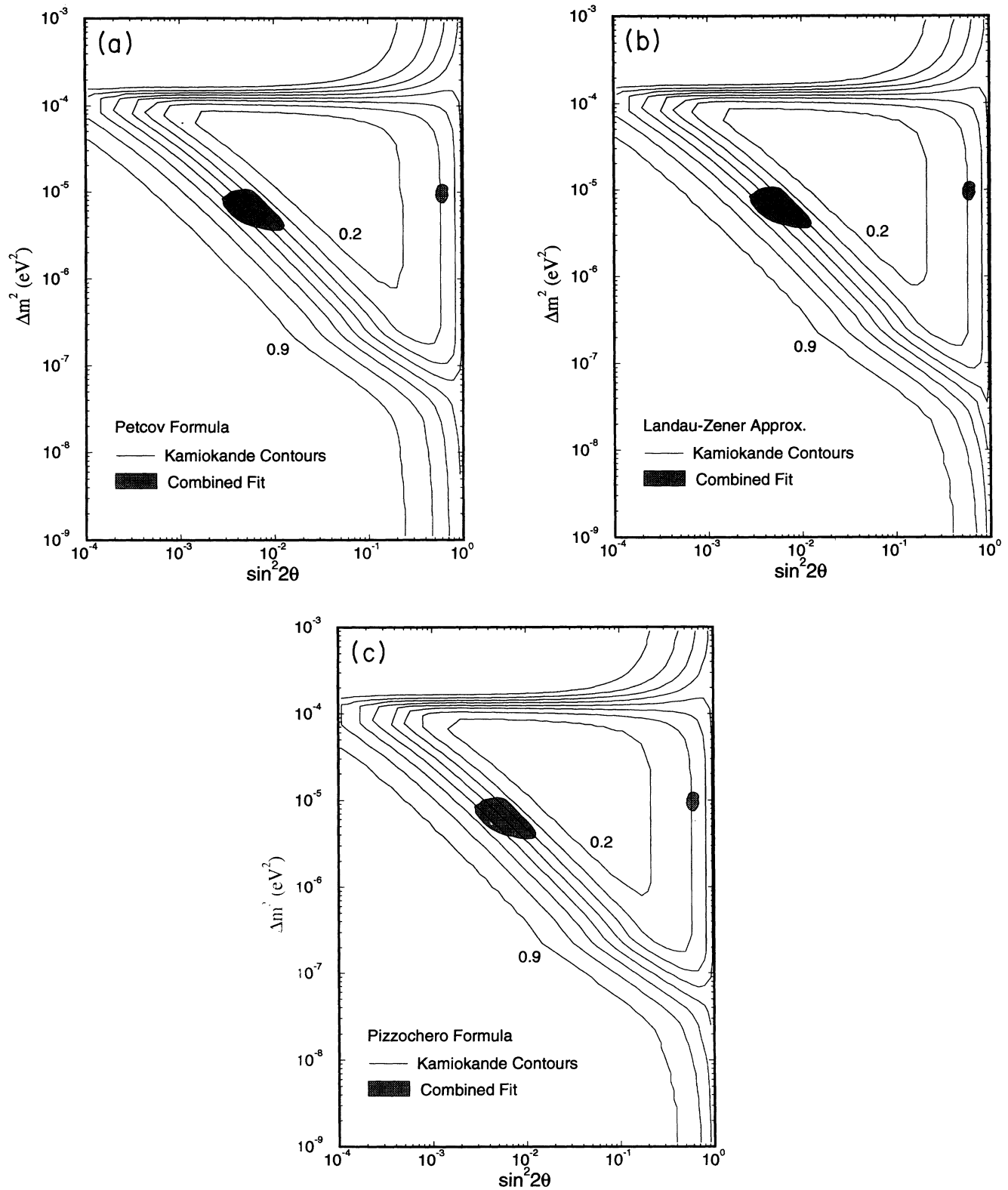
FIG. 9. The Kamiokande contours of the signal to SSM ratio (including the neutral current reaction in flavor oscillations) for three different analytic MSW approximations of (a) Petcov, (b) Parke, and (c) Pizzochero. The Earth effect is not included. The formulas by Parke and Pizzochero fail in the large-angle, small Δm^2 region ($\Delta m^2 \leq 3 \times 10^{-8} \mathrm{eV}^2$). Also shown are the allowed regions of the combined observations including the Earth effect and the Kamiokande day-night data. We show the Kamiokande contours without the Earth effect since they involve only the $^8\mathrm{B}$ flux and make a clean comparison possible. The energy resolution and the detector efficiency of Kamiokande are included.

Ref. [23].) This definition can, however, overestimate the allowed regions. Consider, for example, the parameters that are marginally allowed at 95% C.L. by two experiments; if we take the overlap as the combined fit, the parameters are allowed. But the total χ^2 can be very large: χ^2 should be about 12 (= 2 × 6.0) at the edge of the two allowed regions and is allowed only at 99.8% C.L. by the χ^2 analysis. Taking the overlap of the allowed regions of the different experiments displayed in Fig. 10 clearly overestimates the uncertainties when compared to the χ^2 analysis shown in Fig. 5, especially for the large-angle solution. Also the overlap procedure by definition ignores the correlations of the uncertainties between different experiments.

Another C.L. definition used in the literature [20,21] utilizes the 1000 Monte Carlo SSM's. The 95% C.L. is, for example, defined by calculating a χ^2 value for each Monte Carlo SSM and for each $\sin^2 2\theta$ and Δm^2, including only experimental uncertainties and the detector cross-section uncertainties. If 50 of the 1000 Monte Carlo SSM's satisfy

$$\chi^2(\sin^2 2\theta, \Delta m^2; \text{Monte Carlo}) \leq \chi^2_{\min}(\text{central}) + 6.0,$$

$$(20)$$

FIG. 10. The combined allowed regions are simply taken as overlaps of the three experimental constraints at 95% C.L. This C.L. definition overestimates the uncertainties, allowing a parameter space which is marginally allowed by different experiments, but, in fact, its χ^2 is large and the combined fit is poor. As a result the obtained parameter space is significantly overestimated compared to Fig. 5, especially in the large-angle region; even a third allowed region appears in large-angle, small Δm^2. Also this overlap procedure ignores uncertainty correlations between different experiments.

FIG. 11. The allowed regions of the combined experiments using different C.L definitions; (a) the Monte Carlo SSMs, (b) the Monte Carlo SSMs using the overlap of the experimental and theoretical uncertainties [20,21]. The latter method overestimates the allowed regions.

this parameters space is allowed. [χ^2_{min}(central) is the global minimum of χ^2 when the central values of the SSM fluxes are used.] This method is, however, statistically incorrect since it essentially takes the overlap of experimental uncertainties and theoretical uncertainties. It therefore overestimates the allowed region for the same reason as the overlapping of the allowed regions from different experiments. We believe the most statistically rigorous usage of the Monte Carlo SSM's is given by Eq. (16). The allowed regions obtained by Eqs. (16) and (20) are shown in Fig. 11.

Before improving the statistical definition of the uncertainties of the obtained parameters, we consider the goodness-of-fit for each MSW solution under the MSW hypothesis: if one of the MSW solutions is true, then how likely is it to obtain the observed (or a larger) χ^2? The goodness-of-fit is calculated from the χ^2 minimum for each MSW solution. Without the Earth effect, the χ^2 minimum of the nonadiabatic and large-angle solution are 0.5 and 4.9, respectively. For 1 degree of freedom (= 3 experiments − 2 parameters), the probabilities of obtaining the χ^2 values equal to or larger than those χ^2 values by chance are 48% and 3%, respectively. That is, the hypothesis that the nonadiabatic solution is the true solution yields a good fit, while the large-angle solution hypothesis is possible statistically only at 3%. When the Earth effect and the Kamiokande II day-night result (6 data points) are included, there is a third χ^2 minimum in the large-angle region with $\sin^2 2\theta = 0.76$ and $\Delta m^2 = 1.2 \times 10^{-7}\,\text{eV}^2$, because of the regeneration of the electron neutrinos in the Earth at night in the pp and ^{7}Be energy range. The χ^2 values are 3.1, 8.1, and 13.1 for the nonadiabatic, large-angle, and new large-angle solution, respectively. For 7 degrees of freedom (= 9 data − 2 parameters), the probabilities of getting χ^2 larger than those values are 88, 32, and 7%. The fits for the first two solutions are reasonable, while the third fit is somewhat poor but not excluded. The small χ^2 contribution from the Kamiokande day-night data is responsible for the improvement of the large-angle, large Δm^2 solution. The results are summarized in Tables VIII and IX and the corresponding results for sterile neutrinos in Tables X and XI.

TABLE VIII. The best fit values of the MSW parameters when the Earth effect is ignored. The SSM uncertainties and their correlations are included by the parametrized method. P is the goodness of fit, i.e., the probability of obtaining by chance a χ^2 equal to or larger than the obtained χ^2. $P_{relative}$ is the relative probability between the different solutions when the probability distribution is Gaussian for each solution. The improved definition of 90, 95, and 99 % C.L. correspond to $\Delta \chi^2 = 5.9, 7.3$, and 10.6 [see Fig. 12(a)].

	Nonadiabatic	Large angle I
$\sin^2 2\theta$	6.4×10^{-3}	0.71
Δm^2 (eV^2)	6.3×10^{-6}	1.6×10^{-5}
χ^2 (1 DF)	0.5	4.9
P (%)	48	3
$P_{relative}$ (%)	89	11

TABLE IX. Same as Table VIII except that the Earth effect and the Kamiokande II day-night effect are included. The improved definition of 90, 95, and 99 % C.L. correspond to $\Delta \chi^2 = 5.5, 7.0$, and 10.9 [see Fig. 12(b)].

	Nonadiabatic	Large angle I	Large angle II
$\sin^2 2\theta$	6.5×10^{-3}	0.62	0.76
Δm^2 (eV^2)	6.1×10^{-6}	9.4×10^{-6}	1.2×10^{-7}
χ^2 (7 DF)	3.1	8.1	13.1
P (%)	88	32	7
$P_{relative}$ (%)	94.9	4.6	0.5

The nonadiabatic solution gives a better fit than the large-angle solutions, either with or without the Earth effect, and this tendency can be quantified in another way: suppose the two-flavor MSW is true and the probability density of finding the true parameter is distributed throughout the $\log \sin^2 2\theta - \log \Delta m^2$ plane, including all the χ^2 minima. That is, we assume that the probability distribution is

$$P(\sin^2 2\theta, \Delta m^2) = N \exp[-\chi^2(\sin^2 2\theta, \Delta m^2)/2], \quad (21)$$

where N is chosen so that the total probability is unity. Then what is the relative probabilities of finding the true parameters in the different regions? We approximate the probability distributions as an overlap of Gaussian distributions, each corresponding to a different MSW region. Then the relative probability of finding the true parameters in the ith region (i = nonadiabatic, large-angle solutions) is calculated as

$$P^i_{relative} = \frac{2\pi\sigma^i_s\sigma^i_m\sqrt{1-\rho^{i2}}\exp(-\chi^2_{i,min}/2)}{\sum_j 2\pi\sigma^j_s\sigma^j_m\sqrt{1-\rho^{j2}}\exp(-\chi^2_{j,min}/2)}, \quad (22)$$

where σ_s and σ_m are the standard deviations of $\log \sin^2 2\theta$ and $\log \Delta m^2$, respectively, and ρ^i is the correlation parameter; j runs over each allowed region with the χ^2 minimum $\chi^2_{j,min}$. Without the Earth effect, the relative probabilities of finding the true parameters in the nonadiabatic and large-angle region are 89% and 11%, respectively. When the Earth effect and the Kamiokande II day-night data are included, the probabilities for the nonadiabatic and two large-angle solutions are 94.9%, 4.6%, and 0.5%, respectively. The nonadiabatic solution is strongly favored. The results are summarized in

TABLE X. Same as Table VIII except that the oscillations are for sterile neutrinos. The Earth effect and the Kamiokande II day-night effect are not included. The improved definition of 90, 95, and 99 % C.L. correspond to $\Delta \chi^2 = 4.8, 6.5$, and 10.6.

	Nonadiabatic	Large angle I
$\sin^2 2\theta$	7.4×10^{-3}	0.85
Δm^2 (eV^2)	4.7×10^{-6}	9.6×10^{-6}
χ^2 (1 DF)	2.8	11.7
P (%)	9.4	0.06
$P_{relative}$ (%)	98.9	1.1

TABLE XI. Same as Table X except that the Earth effect and the Kamiokande II day-night effect are included. The improved definition of 90, 95, and 99 % C.L. correspond to $\Delta\chi^2 = 4.6$, 6.0, and 9.1.

	Nonadiabatic	Large angle I	Large angle II
$\sin^2 2\theta$	7.0×10^{-3}	0.77	0.60
Δm^2 (eV^2)	4.5×10^{-6}	6.7×10^{-6}	6.9×10^{-8}
χ^2 (7 DF)	7.0	21.0	24.2
P (%)	43	0.4	0.1
P_{relative} (%)	99.59	0.03	0.01

Tables VIII and IX.

Finally, using the probability density approximated with multiple Gaussian distributions, we improve the confidence level definition of the MSW parameter uncertainties. The confidence level P and $\Delta\chi^2$ are related by

$$P(\Delta\chi^2) = \frac{\sum_i 2\pi \sigma_s^i \sigma_m^i \sqrt{1 - \rho^{i2}} \, \mathcal{P}_i(\Delta\chi^2)}{\sum_j 2\pi \sigma_s^j \sigma_m^j \sqrt{1 - \rho^{j2}} \exp(-\chi_{j,\min}^2/2)}, \quad (23)$$

where

$$\mathcal{P}_i(\Delta\chi^2) = \int_{\chi_{i,\min}^2}^{\chi_{0,\min}^2 + \Delta\chi^2} \exp[-\tfrac{1}{2}(\chi_{0,\min}^2 + \chi^2 - \chi_{i,\min}^2)] \, d\chi^2 \quad (24)$$

with $\chi_{0,\min}^2 = \min\{\chi_{i,\min}^2 \mid i = \text{all local minima}\}$. Without the Earth effect, the 90, 95, and 99 % C.L. correspond to $\Delta\chi^2 = 5.9$, 7.3, and 10.6, respectively. With the Earth effect, $\Delta\chi^2 = 5.5$, 7.0, and 10.9. (These should correspond with the values $\Delta\chi^2 = 4.6$, 6.0, and 9.2 for a single Gaussian distribution.) We believe that the new prescription is more reliable because it takes into account the existence of multiple minima and our lack of a priori knowledge of which is the true solution. It is also a more conservative estimate of the uncertainties. The allowed regions with the improved C.L. definition are shown in Fig. 12.

D. Results of the global MSW analysis

The results of the global MSW analysis for two-flavor oscillations are displayed in Fig. 13 and the best fit parameters are listed in Tables IX. These include the parametrized SSM uncertainties and their correlations, the Earth effect and the Kamiokande II day-night data, the improved statistical definition of confidence levels, and the updated experimental input data.[10] Between

[10]There are additional Kamiokande II data of the energy spectrum of recoil electrons [3]. The spectrum slightly disfavors a part of the adiabatic region ($\Delta m^2 \sim 10^{-4}$ eV^2 and $\sin^2 2\theta \sim 6 \times 10^{-3}$), but the effect in the combined fit is insignificant. The spectrum information is not statistically independent and is therefore not included in our analysis.
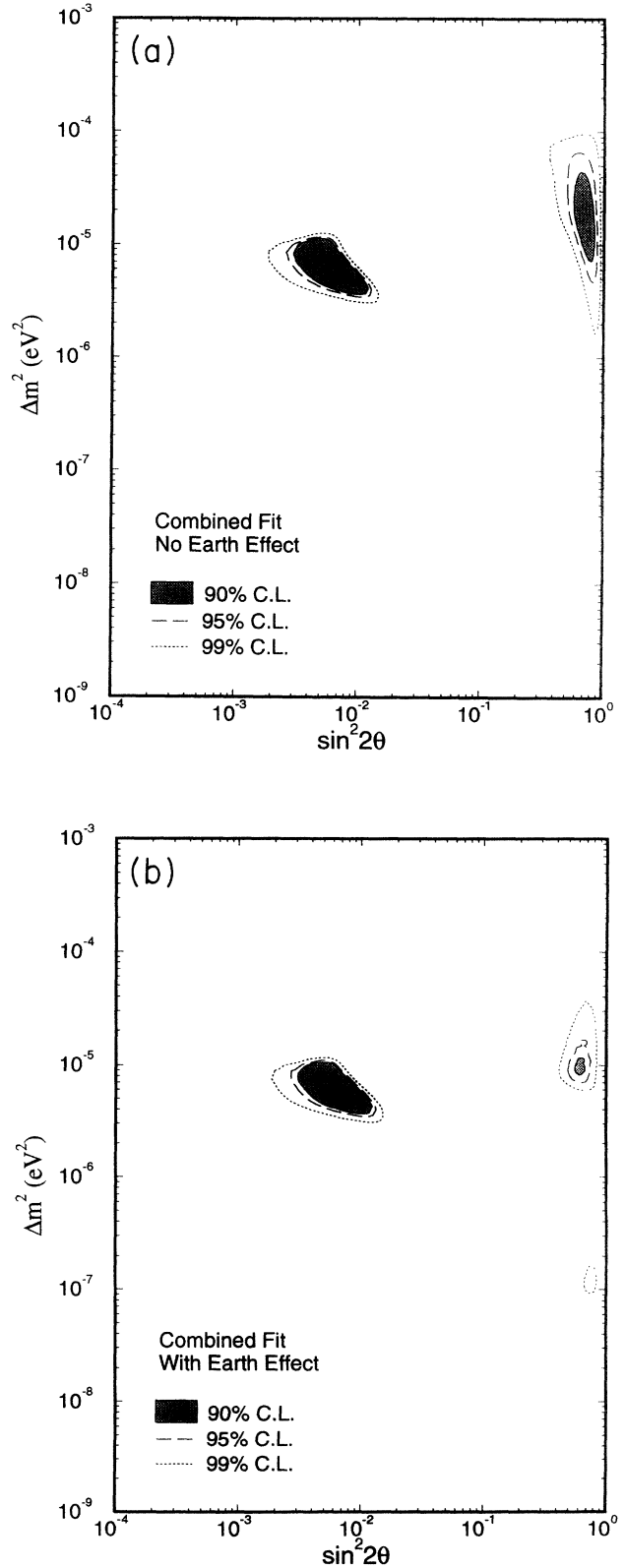
FIG. 12. The allowed regions of the combined experiments using an improved C.L definition that assumes a Gaussian probability density for each solution. The 90, 95, and 99 % C.L. correspond to (a) $\Delta\chi^2 = 5.9$, 7.3, and 10.6, ignoring the Earth effect and (b) $\Delta\chi^2 = 5.5$, 7.0, and 10.9, including the Earth effect.

FIG. 13. The updated result of the combined MSW analysis assuming the Bahcall-Pinsonneault SSM. The Earth effect, Kamiokande II day-night data, theoretical uncertainties and their correlations of the parametrized method are included, and the improved C.L. definition is used.
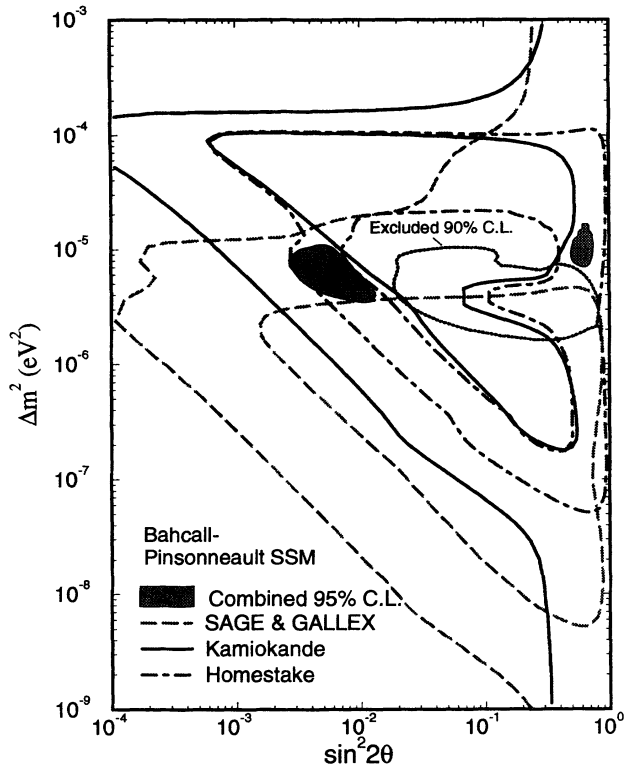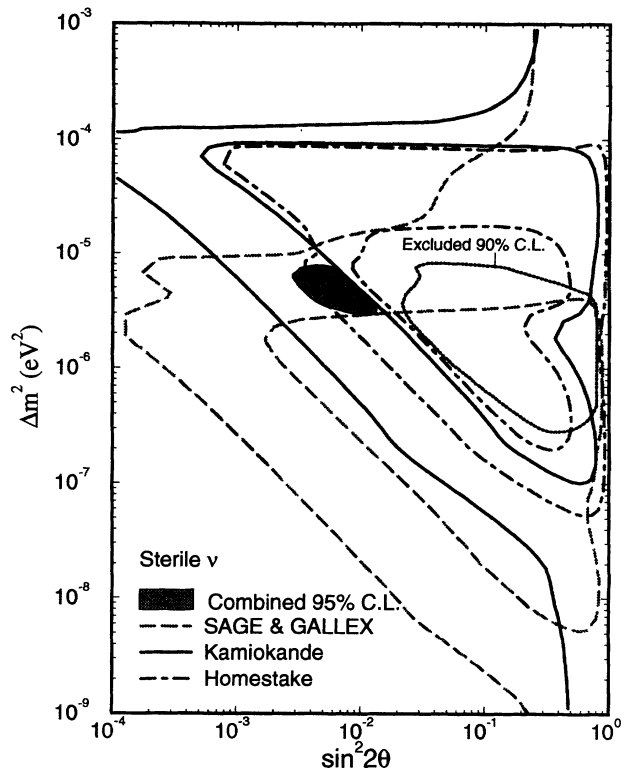
FIG. 14. The updated result of the combined MSW analysis for the oscillations into sterile neutrinos. The Bahcall-Pinsonneault SSM is assumed. The Earth effect, Kamiokande II day-night data, theoretical uncertainties and their correlations of the parametrized method are included, and the improved C.L. definition is used.

the two allowed regions at 90% C.L., the nonadiabatic solution with

$$\Delta m^2 \sim 6 \times 10^{-6} \, \text{eV}^2 \quad \text{and} \quad \sin^2 2\theta \sim 7 \times 10^{-3} \quad (25)$$

gives an excellent description of the observations, while the second (large-angle) solution with

$$\Delta m^2 \sim 9 \times 10^{-6} \, \text{eV}^2 \quad \text{and} \quad \sin^2 2\theta \sim 0.6 \quad (26)$$

is marginally allowed at 90% C.L. In the second region the Earth effect and the uncertainty correlations between the experiments are significant: the regeneration of ν_e in the Earth during the night distorts and enlarges the allowed region, while the absence of the day-night asymmetry in the Kamiokande II data excludes a wide parameter space [19,31,41]. The omission of the correlation would result in overestimating the uncertainties. There is also a third solution at large-angle and low Δm^2 that is allowed at 99% C.L. when the Earth effect, which in this region is significant for the pp and ^{7}Be fluxes, is included.

One can consider the MSW oscillation to sterile neutrinos instead of ν_μ or ν_τ. In that case the survival probability of electron neutrinos depends both on the electron and neutron density in the Sun [18,27,44]. A more important difference is the lack of a neutral current contribution in the Kamiokande experiment, which would amount to about 15% of the total signal for fla-

vor oscillations, requiring a larger ν_e survival probability in the sterile neutrino case. As a result the MSW effect now cannot completely resolve the larger Kamiokande rate relative to that of Homestake, and the fit becomes poorer, especially for the large-angle (with large Δm^2) solution. There, $\chi^2_{\min}$ is 21.0 for 7 degrees of freedom including the Earth effect, and no allowed region exists even at 99% C.L. (see Figs. 14 and 15, Tables X and XI). The large-angle region for sterile neutrinos is independently excluded by the bound on the number of neutrino species in big-bang nucleosynthesis [44,45].

IV. THE MSW EFFECT IN NONSTANDARD SOLAR MODELS

We have so far considered the MSW effect within the SSM uncertainties. The SSM is, however, still a theory that needs to be calibrated. Although the nonstandard solar models alone cannot explain the solar neutrino data [16], it is possible that the MSW effect takes place while the SSM is incorrect. We have examined constraints on the MSW parameter space with four different nonstandard solar models that are explicitly calculated and have neutrino flux predictions. (No flux uncertainties are given in those models and we assume the standard values of the uncertainties in Ref. [8].) Each of
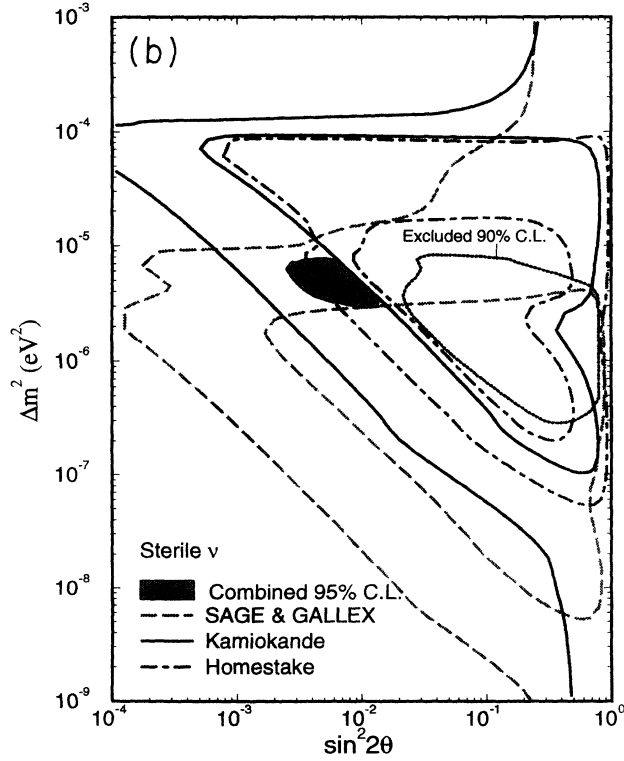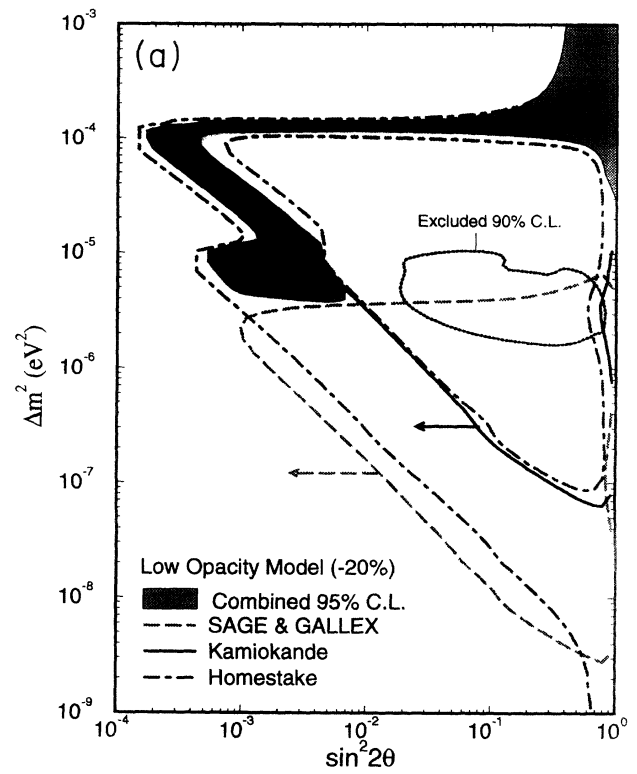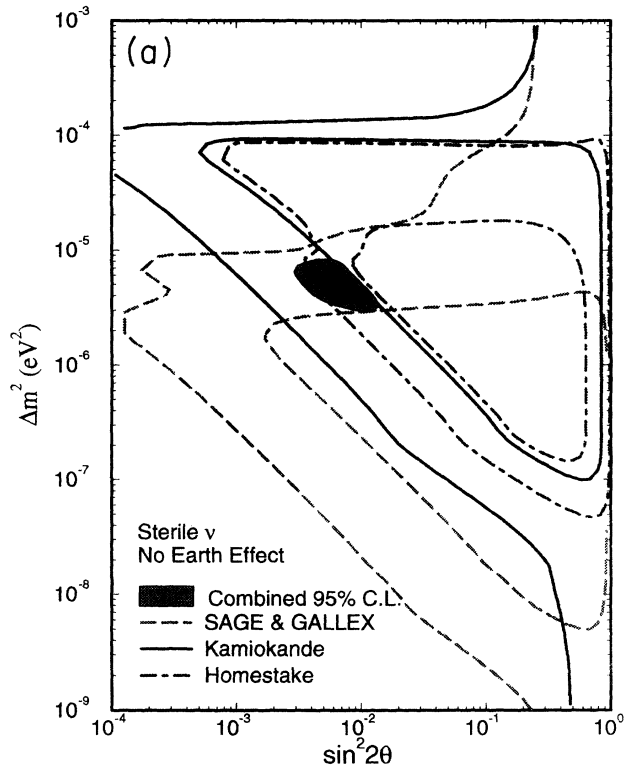
FIG. 15. The combined allowed regions for oscillations into sterile neutrinos (a) without and (b) with the Earth effect. No solutions are allowed in the large-angle regions even at 99% C.L.

FIG. 16. The experimental constraints assuming nonstandard solar models that predict neutrino fluxes *smaller* than the SSM: (a) the opacity is reduced by 20% at temperature larger than 5×10^6 K [46], (b) S_{11} is increased by 30% [14].
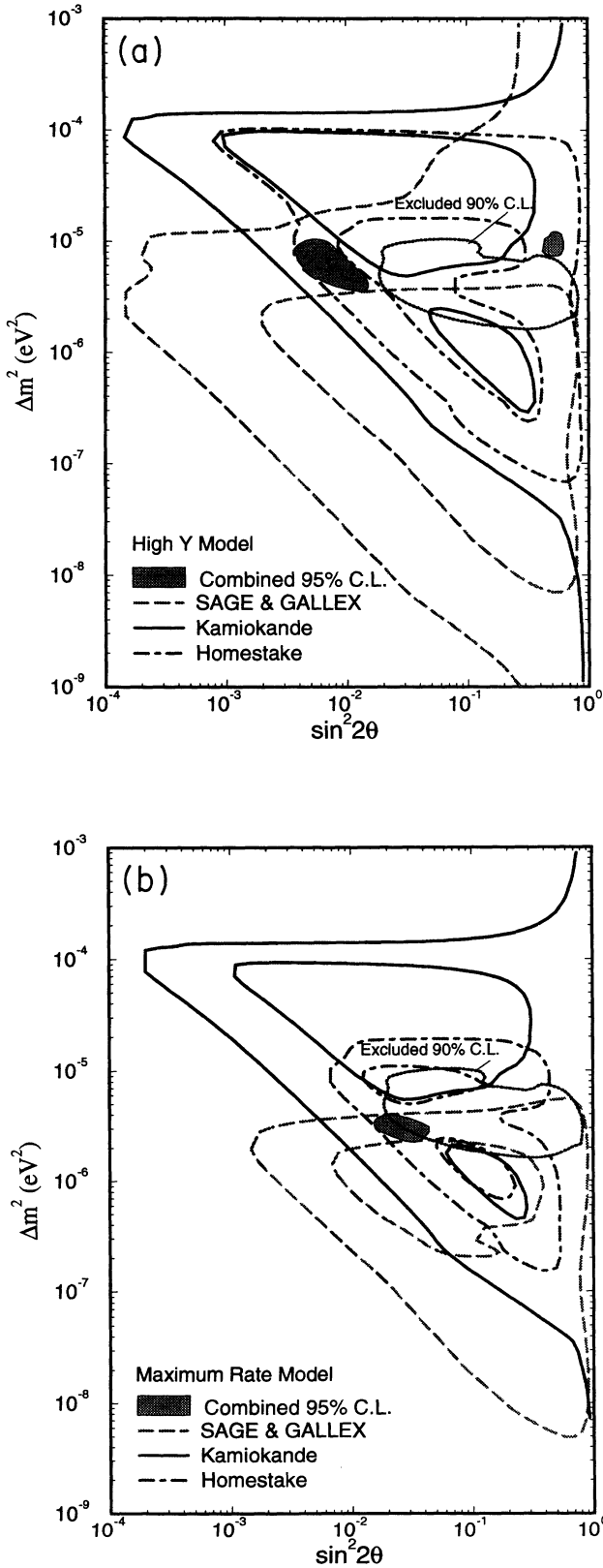
FIG. 17. The experimental constraints assuming nonstandard solar models that predict neutrino fluxes *larger* than the SSM: (a) a high Y model [27,28] and (b) the maximum rate model in which S_{33} is artificially set to zero, maximizing the gallium rate to 303 SNU [8].

these models is *ad hoc* and assumes nonstandard input parameters that are grossly different from those in the SSM's, addressing possibilities of our ignorance of the astrophysical quantities such as the opacity or the primordial element abundances, or of the nuclear reaction cross sections that have never been measured at energies equivalent to the solar temperature. Two of them were constructed in attempts to explain the solar neutrino deficit, and predict smaller ^8B and ^7Be fluxes than the SSM's: the low opacity model by Dearborn [46], in which the opacity is reduced by 20% in the region where the solar temperature is above 5×10^6 K, and the high S_{11} model with the $p + p$ cross section increased by 30% [14]. The allowed regions are generally enlarged compared to the SSM case, and even the adiabatic branch of ^8B ($\Delta m^2 \sim 10^{-4}$ eV^2 and $\sin^2 2\theta \sim 10^{-4}-1$) is allowed. The MSW parameters for the two models are shown in Figs. 16(a) and (b).

The two other nonstandard solar models predict larger neutrino fluxes: the high Y model [27,28] that assumes a larger primordial helium abundance in the solar interior, considered to solve problems with helioseismology data, and the maximum rate model [8], in which S_{33} is artificially set to zero, yielding the largest prediction for the

FIG. 18. The allowed regions of the combined observations when the central temperature (T_C) is a completely free parameter. The combined data constrain T_C to 1.02 ± 0.02 (1σ), which is consistent with the SSM ($T_C = 1 \pm 0.006$). Also displayed is the region excluded by the Kamiokande day-night data at 90% C.L.; the exclusion comes from the comparison between the different time bins, and is insensitive to the absolute ^8B flux or T_C.

FIG. 19. The experimental constraints when nonstandard S_{17} values are assumed. S_{17} is directly proportional to the ^{8}B flux and has the largest uncertainty among the SSM input parameters. We take S_{17} to be (a) 30% smaller than the SSM, (b) 50% larger than the SSM. In (c) the ^{8}B flux is treated as a completely free parameter; the combined data constraint ^{8}B $= 1.43 + 0.65 - 0.42$ of the standard value (1σ) with $\chi^2_{min} = 2.0$ for 6 degrees of freedom. Also shown in (c) is the excluded region from the Kamiokande II day-night data (90% C.L.), which is independent of the ^{8}B flux magnitude.

SOLAR MODEL UNCERTAINTIES, MSW ANALYSIS, AND ...

gallium rate solar neutrino units [303 (SNU)]. With the larger fluxes the combined allowed regions generally move inward in the MSW triangle, as displayed in Figs. 17(a) and (b).

The solar models with a nonstandard opacity value or nonstandard heavy element abundance are generally parametrized by a nonstandard central temperatures (T_C) [16,11,12], and the neutrino fluxes are described by the power laws of Eq. (1). One can constrain the MSW parameter space from the combined data for these generic nonstandard solar models by allowing T_C to change freely. The allowed MSW regions are displayed in Fig. 18. The existing observations constrain

$$T_C = 1.02 \pm 0.02 \ (1\sigma), \qquad (27)$$

with $\chi^2_{\min} = 2.1$ for 6 degrees of freedom (DF); the T_C obtained by observations allowing the MSW effect is consistent with the SSM $(T_C = 1 \pm 0.006)$. We note that without the MSW effect there is no consistent T_C to describe the observations [12,11,16].

Another major source of uncertainty in the SSM is the $p + {}^7\text{Be}$ cross section (S_{17}), which is poorly measured and has the largest uncertainty among the SSM input parameters. S_{17} is directly proportional to the ${}^8\text{B}$ flux and is independent of the astrophysical uncertainties parametrized by T_C. We have carried out MSW fits assuming two extreme values of S_{17}; a 30% reduction and a 50% increase. (The ${}^8\text{B}$ flux uncertainty is set to zero in the calculation. The standard values are used for the other uncertainties.) The results are shown in Figs. 19(a) and (b). It is also reasonable to consider the ${}^8\text{B}$ flux as a free parameter, given the large uncertainties from both astrophysics and nuclear physics. When the ${}^8\text{B}$ flux is used as a completely free parameter in the MSW fit, the experiments constrain

$$\phi(\text{B})/\phi(\text{B})_{\text{SSM}} = 1.43 + 0.65 - 0.42 \ (1\sigma) \qquad (28)$$

with $\chi^2_{\min} = 2.1$ for 6 DF, and the allowed regions are displayed in Fig. 19(c). The larger values of $\phi(\text{B})$ and T_C are preferred since a larger ${}^8\text{B}$ flux can reduce the relative difference in the survival probabilities for Homestake and Kamiokande, giving more freedom in the MSW parameter constraint.

V. MSW PREDICTIONS FOR FUTURE EXPERIMENTS

One can check the consistency between the current observations and the MSW theory by predicting the gallium rate from the combined chlorine and Kamiokande data [47]. The parameter space allowed by the two experiments is shown in Fig. 20(a), along with the survival probability contours for the gallium experiment. Assuming the Bahcall-Pinsonneault SSM, the combined Homestake and Kamiokande observations predict the gallium rate to be ≤ 100 SNU; the MSW prediction is consistent with the current result of SAGE and GALLEX albeit the large theoretical uncertainty. By reducing the statistical uncertainties, we estimate the allowed parameter space
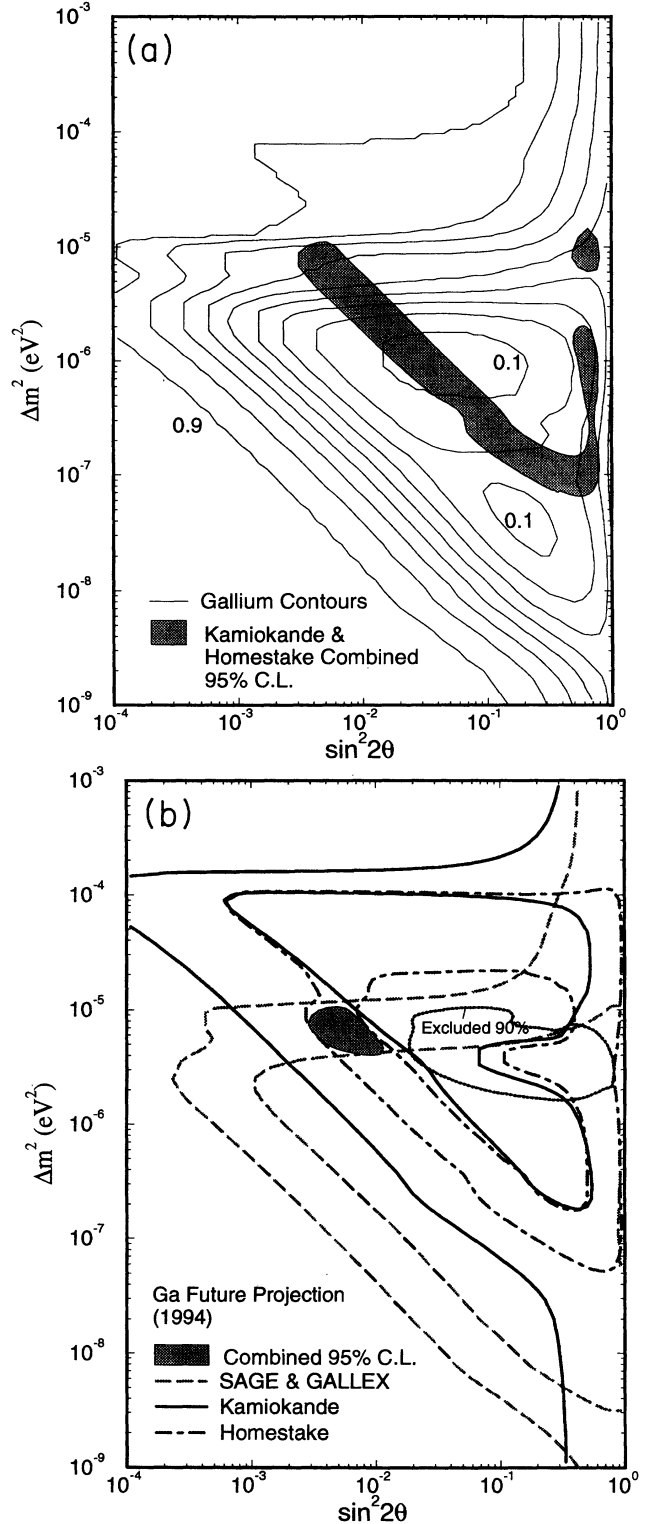

FIG. 20. (a) The combined result of the Homestake and Kamiokande experiments. From the allowed regions we can predict the gallium rate to be ≤ 100 SNU at 95% C.L., which is consistent with the current observations of SAGE and GALLEX. (b) The combined result when the gallium experimental uncertainty is reduced by a factor $1/\sqrt{2}$, which is equivalent to the data set through the end of 1994. The central value of the gallium rate is assumed to stay at the current value. The present values are used for the other experiments.

expected in the near future. Shown in Fig. 20(b) is the region allowed by the combined observations when the gallium statistical uncertainty is reduced by a factor $1/\sqrt{2}$, which is equivalent to the data set of the gallium experiment by the end of 1994; the central value is assumed to be the same as current data. Although the nonadiabatic region shrinks somewhat and the large-angle solution is no longer allowed at 95% C.L., no significant change is expected unless the experimental values change drastically.

Although the current observations are consistent with the two-flavor MSW hypothesis and strongly disfavor the astrophysical solutions, a smoking gun evidence for a nonstandard neutrino physics is still awaited. Theoretical questions yet to be answered are (a) distinguishing astrophysical solutions and particle physics solutions (e.g., the MSW effect), (b) calibrating solar models, and (c) distinguishing the MSW nonadiabatic and large-angle solution and extracting Δm^2 and $\sin^2 2\theta$ from the data.

For the next-generation solar neutrino experiments, such as Sudbury Neutrino Observatory (SNO) [48], Super-Kamiokande [49], BOREXINO [50], and Imaging of Cosmic and Rare Underground Signals (ICARUS) [51], the MSW mechanism can yield robust predictions and is a verifiable hypothesis. The measurement of the charged to neutral current ratio (X_{CC}/X_{NC}) in SNO and the measurements of the neutrino energy spectrum and the day-night effect in SNO and Super-Kamiokande should be able to answer the questions addressed above.

The measurement of the neutral current in SNO is insensitive to flavor oscillations and is a direct measurement of the ^{8}B flux. One can calibrate the core temperature of
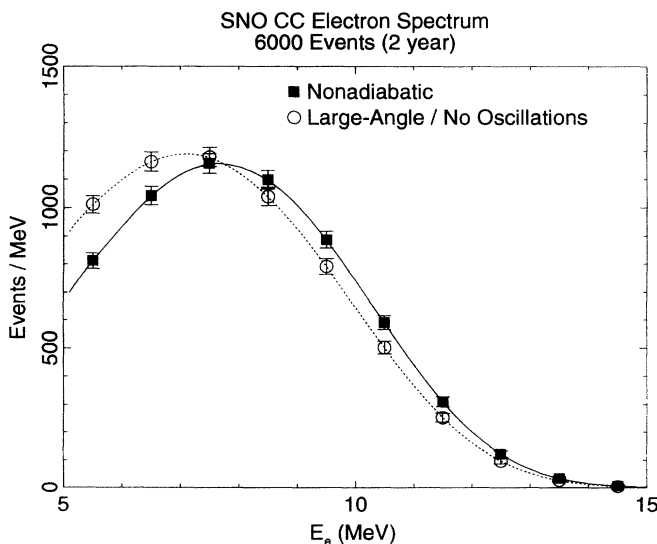

SNO CC Electron Spectrum
6000 Events (2 year)

FIG. 21. The SNO charged current spectrum expected for the nonadiabatic and large-angle solution. To compare the difference, the large-angle spectrum is normalized to the the nonadiabatic. The spectrum shape of astrophysical solutions (i.e., no oscillations) is identical to the large-angle spectrum at the scale of the figure. The charged current cross section [52,53] and the detector resolution [48] are included. The error bars indicate the statistical uncertainties from 6000 events (equivalent to two years of operation).

the Sun at the 1% level given the power-law dependence of the flux ($\phi(B) \sim T_C^{18}$) and allowing a 20% uncertainty from the experimental error and the S_{17} uncertainty.

The measurement of X_{CC}/X_{NC} in SNO would be the most direct test of the MSW hypothesis. The up-to-date global analysis predicts the ratio to be

$$X_{CC}/X_{NC} = \begin{cases} 0.2 - 0.6 & \text{(nonadiabatic solution)} , \\ 0.2 - 0.3 & \text{(large-angle solution)} , \end{cases}$$

(29)

compared to the ratio expected if no oscillations occur. This measurement is, however, insensitive to oscillations between electron neutrinos and sterile neutrinos.

The measurements of the charged current spectrum in SNO and the recoil electron spectrum in Super-Kamiokande are important for distinguishing the two solutions suggested by the global analysis of current observations. Should the nonadiabatic solution, which gives the better fit for the data, be the case, we expect a depletion of electron neutrinos in the lower end of the observed spectrum, while little distortion is expected in the large-angle solution (or for astrophysical solutions). In Fig. 21, we compare the spectra of the two solutions, one in the best fit solution in the nonadiabatic region, and one in the large-angle region. The large-angle spectrum is normalized to the nonadiabatic spectrum above the threshold. The spectrum shape of the large-angle solution is essentially identical to that of the astrophysical solutions (i.e., no oscillations). The error bars indicate the statistical uncertainties assuming 6000 events, equivalent to two years of operation. We have included in the calculation the charged current cross section [52,53] and the detector energy resolution [48].[11] In Fig. 22, the spectra of the two solutions are shown for 16 000 events (two year operation) in Super-Kamiokande. The nonadiabatic solution predicts more significant depletions of neutrinos at lower energy, and therefore the detector sensitivity in the 5 - 7 MeV range is crucial in detecting the spectrum distortion in both SNO and Super-Kamiokande. The spectrum shape expected for oscillations to sterile neutrinos are almost identical to these.

Another MSW prediction that helps to distinguish the two solutions is the day-night effect due to matter oscillations in the Earth during the night. The effect shows up not only in day-night differences of signals, but also in the time dependence during the night and in seasonal variations due to the obliquity of the Earth. The large-angle solutions are quite sensitive to the Earth effect, but the nonadiabatic solution is insensitive at the observable

---

[11]In the spectrum shape analysis it is important to include the effect of the continuous out-coming electron spectrum and the effect the detector resolution. In particular the approximation with a δ function for the electron spectrum from mono-energetic neutrinos (i.e., electron energy = neutrino energy - 1.44 MeV) significantly overestimates the sensitivity for spectrum distortions and is inappropriate for the shape analysis.

Super-Kamiokande Electron Spectrum
16000 Events (2 year)

■ Nonadiabatic
○ Large-Angle / No Oscillations
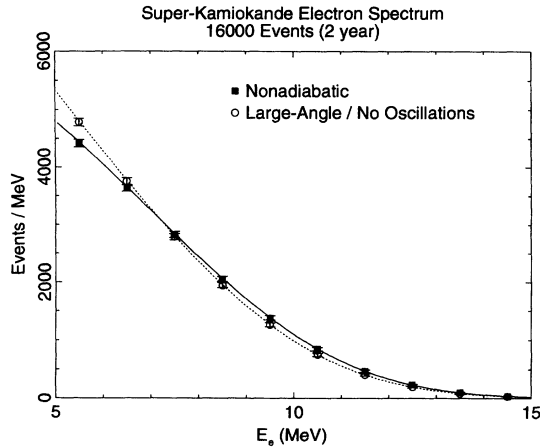
Events / MeV

E_e (MeV)

FIG. 22. The Super-Kamiokande electron spectrum expected for the nonadiabatic and large-angle solutions. To compare the difference, the large-angle spectrum is normalized to the the nonadiabatic. The spectrum shape of astrophysical solutions (i.e., no oscillations) is identical to the large-angle spectrum at the scale of the figure. The detector resolution is included [49]. The error bars indicate the statistical uncertainties from 16 000 events (equivalent to a two year operation).

level.[12] The expected rates at night along with the daytime rate are shown in Figs. 23 and 24 for SNO and Super-Kamiokande, respectively. The night rate is divided into six bins according to the angle between the Sun and the nadir at the detectors, corresponding to bin neutrinos with different path lengths in the Earth. The effect yields such a noticeable variation in the large-angle region that an updated Kamiokande day-night data might be enough to confirm or rule out the large-angle solution. The prediction for Kamiokande with error bars equivalent to 200 events is shown in Fig. 25.

The spectrum distortions and the day-night effect are particularly important for oscillations to sterile neutrinos, for which the charged to neutral current ratio is unchanged by the oscillations and is therefore the same as for astrophysical solutions. The distortion of the spectrum signifies the nonadiabatic solution, while the day-night effect indicates the large-angle solution, which is already excluded at 99% C.L. by the existing data.

When the SSM and two-flavor oscillations are assumed, one can predict the rate in those experiments. In Fig. 26, the combined allowed parameter space is displayed with the survival probability contours of SNO (the charged

current mode), Super-Kamiokande, and BOREXINO. Those high-counting experiments should be able to constrain the parameter space precisely and check the consistency of the MSW predictions.

VI. CONCLUSIONS

Various theoretical uncertainties in the global MSW analysis have been discussed in detail. It was shown that

SNO (CC) Day-Night Data
Nonadiabatic Solution

Rate / SSM

Day   Night   (a)

$cos\delta_{SUN}$

SNO (CC) Day-Night Data
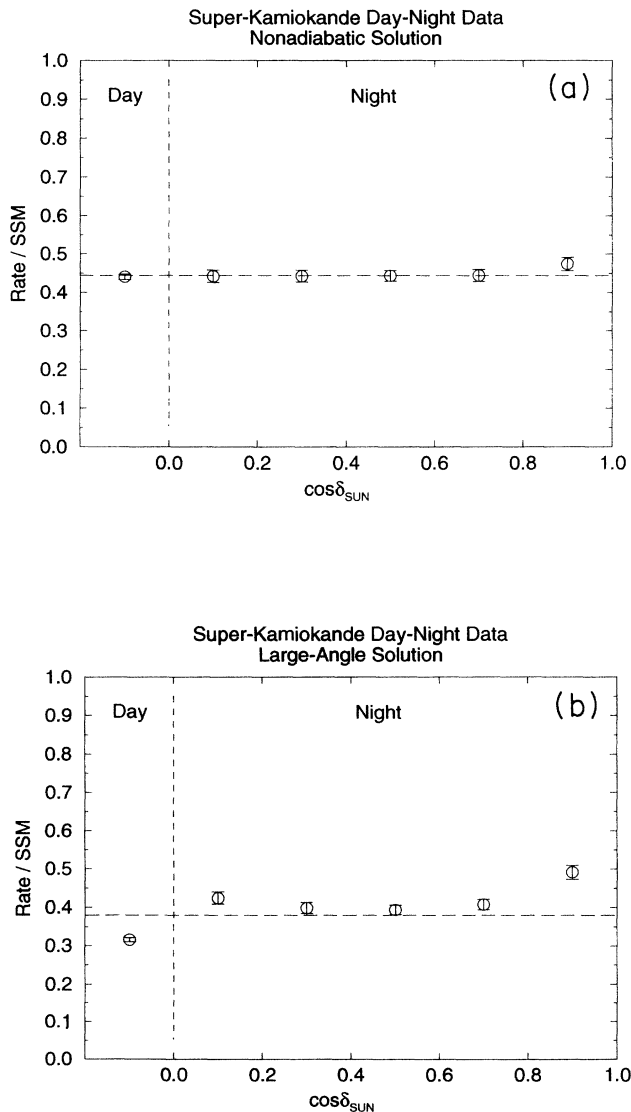Large-Angle Solution

Rate / SSM

Day   Night   (b)

$cos\delta_{SUN}$
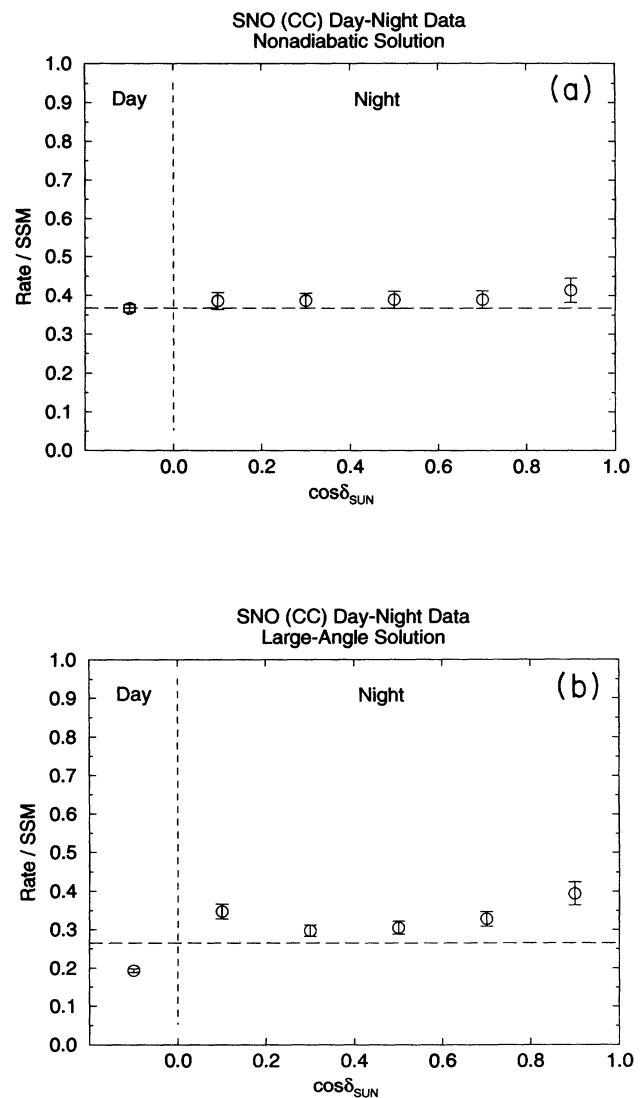
FIG. 23. The Earth effect expected in SNO for the (a) nonadiabatic and (b) large-angle solution. The night rate is shown with five bins according to the angle between the direction to the Sun and the nadir at the detector. The error bars indicate the statistical uncertainties equivalent to one year of operation (3000 events).
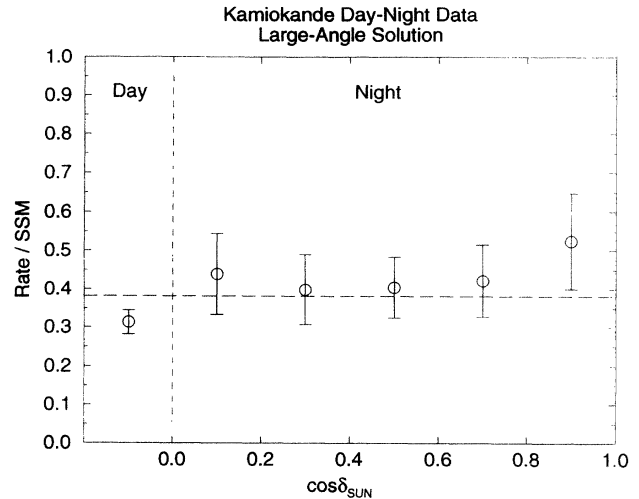
---

[12]A possibility of detecting the day-night effect for the nonadiabatic solution was discussed in Ref. [54]. While it is true that the instantaneous enhancement of the nighttime signal can be ∼ 20% with respect to the daytime signal, it is hardly measurable when the signals are averaged over time bins and the statistical uncertainties are taken into account. See Figs. 23(a) and 24(a).

our parametrized SSM uncertainties yield essentially the same result as the Monte Carlo estimation by Bahcall and Ulrich. The direct comparison was made in the flux uncertainties and their correlations, in the rate uncertainties and their correlations, and in the MSW calculations. The different MSW approximations of Petcov, Parke, and Pizzochero were compared. Various confidence level definitions are discussed and a careful statistical treatment in the global fit was emphasized.

There are two MSW global solutions at 90% C.L., one in the nonadiabatic region and the other in the large-angle, the former solution giving a considerably better

Kamiokande Day-Night Data
Large-Angle Solution

FIG. 25. The Earth effect expected in Kamiokande for the (a) nonadiabatic and (b) large-angle solution. The night time rates are shown with five bins according to the angle between the direction to the Sun and the nadir at the detector. The error bars indicate the statistical uncertainties assuming the total signals of 200 events.

Super-Kamiokande Day-Night Data
Nonadiabatic Solution

Super-Kamiokande Day-Night Data
Large-Angle Solution

FIG. 24. The Earth effect expected in Super-Kamiokande for the (a) nonadiabatic solution and (b) large-angle solution. The night rate is shown with five bins according to the angle between the direction to the Sun and the nadir at the detector. The error bars indicate the statistical uncertainties equivalent to one year of operation (8000 events).

fit. The proper treatment of the Earth effect and the Kamiokande day-night data is significant in the large-angle region. When the Earth effect for the ^{7}Be and pp neutrinos are included, there is a third solution at 99% C.L. in the large-angle, small Δm^2 region. For the oscillations to sterile neutrinos, the solution is limited to the nonadiabatic at 90% C.L. In Fig. 27 the MSW solutions are displayed with other observational hints of neutrino mass: the oscillation interpretation of the atmospheric neutrinos [55] and the cold plus hot dark matter scenario to interpret the Cosmic Background Explorer (COBE) microwave background anisotropy measurement and the large-scale structure observations [56]. The seesaw predictions for neutrino mass and mixing are also displayed in Fig. 27: $\nu_e \leftrightarrow \nu_\mu$ oscillations in the SO(10) grand unified theory (GUT) with an intermediate-scale breaking [11,57], $\nu_e \leftrightarrow \nu_\tau$ oscillations in the supersymmetric SO(10) GUT [11,57], and $\nu_e \leftrightarrow \nu_\mu$ oscillations in the superstring-inspired model with nonrenormalizable operators [58]. In the SO(10) GUT, the ν_τ mass is expected to be in a range relevant to the cosmological hot dark matter. Assuming the Bahcall-Pinsonneault SSM, the MSW solutions for Δm^2 are generally in agreement with the theoretical expectations, especially with the $\nu_e \leftrightarrow \nu_\tau$ oscillations in the supersymmetric SO(10) model. However, the mixing angles are not consistent with the expectation of the simplest versions of the models that the lepton mixing angles are similar to the corresponding quark mixing angles [11]. (For the string-inspired model of Ref. [58] there is no compelling prediction for the mixing angles.)

The global MSW was also carried out for various standard and nonstandard solar models; with the Turck-Chièze–Lopes SSM or nonstandard solar models a wider range of the parameter space is possible. When the core
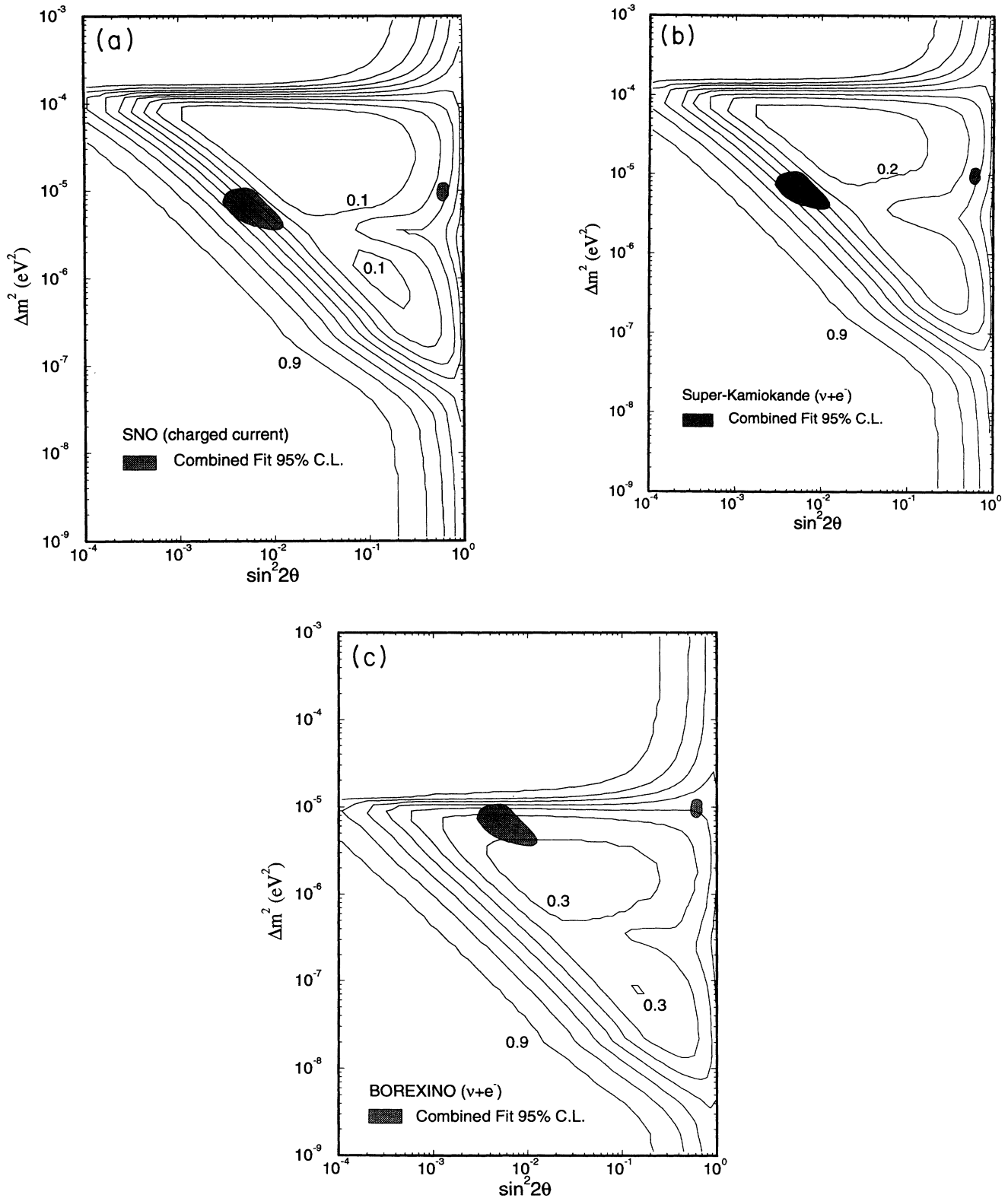
FIG. 26. The contours of the signal to the SSM ratio including the time-averaged Earth effect for (a) the SNO charged current mode $(\nu_e + d \to p + p + e)$, (b) Super-Kamiokande $(\nu e$ scattering), and (c) BOREXINO $(\nu e$ scattering). Superimposed are the combined current allowed regions at 95% C.L of the Homestake, Kamiokande, and gallium experiments.
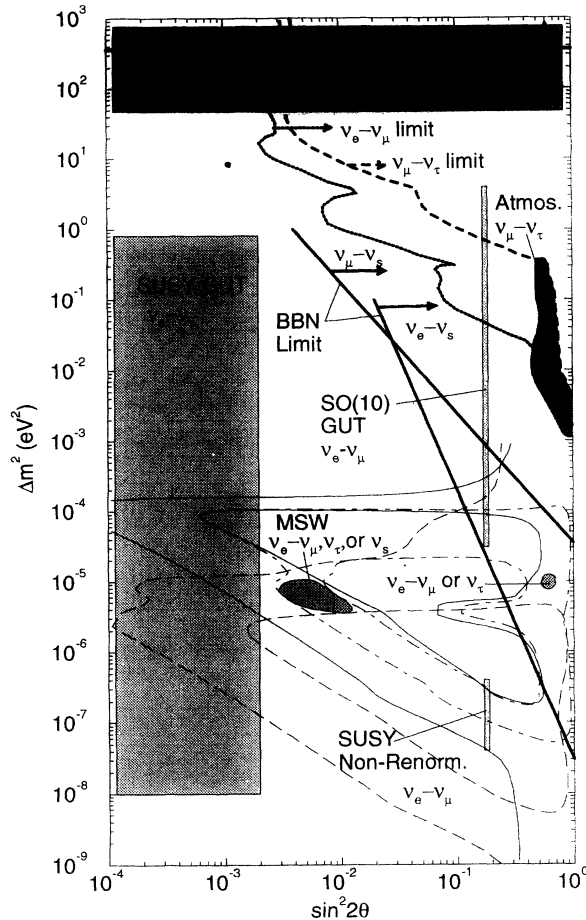
FIG. 27. Shown are the constraints on the $\nu_e \leftrightarrow \nu_\mu$ and $\nu_\mu \leftrightarrow \nu_\tau$ oscillations [59], the constraints on the oscillations into sterile neutrinos ($\nu_e \leftrightarrow \nu_s$ and $\nu_\mu \leftrightarrow \nu_s$) from big-bang nucleosynthesis (BBN) [45], and three observational hints of neutrino mass: the MSW hypothesis for the solar neutrino deficit, the oscillation interpretation of the atmospheric neutrino deficit [55], and the cold plus hot dark matter scenario for the COBE and large scale structure data [56]. Also displayed are predictions from various theoretical models [11,57,58].

temperature and the ^{8}B flux each was used as a free fitting parameter, the data constrained $T_C = 1.02 \pm 0.02$ and $\phi(\text{B})/\phi(\text{B})_{\text{SSM}} = 1.43 + 0.65 - 0.42$ at 1σ, respectively.

The predictions of the MSW solutions assuming the Bahcall-Pinsonneault SSM were discussed in detail for SNO and Super-Kamiokande. We expect for flavor oscillations the charged to neutral current ratio in SNO to be 0.2 – 0.6 and 0.2 – 0.3 of the SSM prediction for the nonadiabatic and large-angle solution, respectively. The nonadiabatic solution yields spectrum distortions measurable in SNO and Super-Kamiokande, while the large-angle solution predicts characteristic day-night differences. The spectrum distortion and the day-night effect are independent of solar models, and are particularly important for the oscillations to sterile neutrinos because the absence of the neutral current in SNO prevents one from distinguishing neutrino oscillations from astrophysical solutions in the charged to neutral current ratio measurement.

Note added. After having finished the first version of the manuscript, we obtained a paper by Fiorentini *et al.* [26], in which the MSW calculations were done with rigorous numerical integrations and the result was compared to our previous work [12], which uses an analytic approximation. The calculations of Ref. [26] do not include the theoretical uncertainties, preventing the authors from exact comparisons. Thanks to M. Lissia and D. Vignaud, we obtained the computer-readable files of their results and we could directly compare our calculations to their Kamiokande contours (Fig. 1(b) of [26]) and their combined allowed regions (Fig. 2(a) of [26]). The agreement between the two calculations was excellent.

ACKNOWLEDGMENTS

[1] R. Davis, Jr. *et al.*, in *Proceedings of the 21th International Cosmic Ray Conference*, edited by R. J. Protheroe (University of Adelaide Press, Adelaide, 1990), Vol. 12, p. 143; R. Davis, Jr., in *Frontiers of Neutrino Astrophysics*, edited by Y. Suzuki and K. Nakamura (Universal Academy, Tokyo, 1993), p. 47.

[2] K. Lande (private communications); B. Cleveland (private communications).

[3] Kamiokande II Collaboration, K. S. Hirata *et al.*, Phys. Rev. Lett. **65**, 1297 (1990); **65**, 1301(1990); **66**, 9 (1991); Phys. Rev. D **44**, 2241 (1991).

[4] A. Suzuki, KEK Report No. 93-96, 1993 (unpublished); Y. Suzuki, in *Frontiers of Neutrino Astrophysics* [1], p. 61.

[5] SAGE Collaboration, A. I. Abazov, *et al.*, Phys. Rev. Lett. **67**, 3332 (1991).

[6] V. N. Gavrin, in 3rd International Workshop on Theory and Phenomenology in Astroparticle and Underground Physics, Assergi, Italy, 1993 (unpublished).

[7] GALLEX Collaboration, P. Anselmann *et al.*, Phys. Lett. B **285**, 376 (1992); **285**, 390 (1992); **314**, 445 (1993).

[8] J. N. Bahcall and M. H. Pinsonneault, Rev. Mod. Phys.

64, 885 (1992).

[9] S. Turck-Chièze and I. Lopes, Astrophys. J. **408**, 347 (1993); S. Turck-Chièze, S. Cahen, M. Cassé, and C. Doom, *ibid.* **335**, 415 (1988).

[10] J. N. Bahcall and H. A. Bethe, Phys. Rev. D **47**, 1298 (1993); Phys. Rev. Lett. **65**, 2233 (1990); H. A. Bethe and J. N. Bahcall, Phys. Rev. D **44**, 2962 (1991).

[11] S. Bludman, D. Kennedy, and P. Langacker, Phys. Rev. D **45**, 1810 (1992); Nucl. Phys. **B374**, 373 (1992).

[12] S. Bludman, N. Hata, D. Kennedy, and P. Langacker, Phys. Rev. D **47**, 2220 (1993).

[13] X. Shi and D. N. Schramm, Fermilab Report No. 92/322-A (to be published in Particle World); D. N. Schramm and X. Shi, Nucl. Phys. B (Proc. Suppl.) (to be published).

[14] V. Castellani, S. Degl'Innocenti, and G. Fiorentini, Phys. Lett. **303**, 68 (1993).

[15] V. Castellani, S. Degl'Innocenti, and G. Fiorentini, Astron. Astrophys. **271**, 601 (1993).

[16] N. Hata, S. Bludman, and P. Langacker, Phys. Rev. D **49**, 3622 (1994).

[17] J. N. Bahcall, Phys. Rev. D **44**, 1644 (1991).

[18] L. Wolfenstein, Phys. Rev. D **17**, 2369 (1978); **20**, 2634 (1979); S. P. Mikheyev and A. Yu. Smirnov, Yad. Fiz. **42**, 1441 (1985) [Sov. J. Nucl. Phys. **42**, 913 (1985)]; Nuovo Cimento **9C**, 17 (1986).

[19] N. Hata and P. Langacker, Phys. Rev. D **48**, 2937 (1993).

[20] J. N. Bahcall and W. C. Haxton, Phys. Rev. D **40**, 931 (1989).

[21] X. Shi, D. N. Schramm, and J. N. Bahcall, Phys. Rev. Lett. **69**, 717 (1992); X. Shi and D. N. Schramm, Phys. Lett. B **283**, 305 (1992).

[22] J. M. Gelb, W. Kwong, and S. P. Rosen, Phys. Rev. Lett. **69**, 1864 (1992).

[23] P. I. Krastev and S. T. Petcov, Phys. Lett. B **299**, 99 (1993).

[24] L. Krauss, E. Gates, and M. White, Phys. Lett. B **299**, 94 (1993). In this paper, the input data of the Kamiokande and Homestake, SAGE, and GALLEX are, respectively, 0.49 ± 0.08, 0.28 ± 0.04, 0.44 ± 0.21, and 0.63 ± 0.16 SSM, which is slightly different from our updated input data (Table I).

[25] G. L. Fogli, E. Lisi, and D. Montanino, Phys. Rev. D **49**, 3626 (1994). G. L. Fogli and E. Lisi, Astropart. Phys. **2**, 91 (1994).

[26] G. Fiorentini *et al.*, Phys. Rev. D **49**, 6298 (1994).

[27] J. N. Bahcall and R. N. Ulrich, Rev. Mod. Phys. **60**, 297 (1988).

[28] J. N. Bahcall, *Neutrino Astrophysics* (Cambridge University Press, Cambridge, England, 1989).

[29] See Fig. 11 of Bahcall and Ulrich [27] and Figs. 6.2 (p. 150) and 6.3 (p. 152) of Bahcall [28].

[30] J. N. Bahcall, in *Proceedings of the XXVI International Conference on High Energy Physics*, Dallas, Texas, 1992, edited by J. Sanford, AIP Conf. Proc. No. 272 (AIP, New York, 1993), Vol. 1, p. 1111.

[31] A. J. Baltz and J. Weneser, Phys. Rev. D **35**, 528 (1987); **37**, 3364, (1988); E. D. Carlson, *ibid.* **34**, 1454 (1986); J. Bouchez, M. Cribier, W. Hampel, J. Rich, M. Spiro, and D. Vignaud, Z. Phys. C **32**, 499 (1986); M. Cribier, W. Hampel, J. Rich, and D. Vignaud, Phys. Lett. B 182, 89 (1986); S. Hiroi, H. Sakuma, T. Yanagida, and M. Yoshimura, Prog. Theor. Phys. **78**, 1428 (1987); A. Dar, A. Mann, Y. Melina, and D. Zajfman, Phys. Rev. D **35**

3607, (1987); P. I. Krastev and S. T. Petcov, Phys. Lett. B **205**, 84 (1988); R. S. Raghavan *et al.*, Phys. Rev. D **44**, 3786 (1991); J. M. LoSecco, *ibid.* **47**, 2032 (1993); V. Barger, K. Whisnant, S. Pakvasa, and R. J. N. Phillips, *ibid.* **22**, 2718 (1980).

[32] See Table XV of Bahcall and Ulrich [27] or Table 7.2 (p. 184) of Bahcall [27].

[33] S. J. Parke, Phys. Rev. Lett. **57**, 1275 (1986).

[34] A. J. Baltz and J. Weneser [31].

[35] W. C. Haxton, Phys. Rev. D **35**, 2352 (1987).

[36] P. Pizzochero, Phys. Rev. D **36**, 2293 (1987).

[37] S. T. Petcov, Phys. Lett. B **200**, 373 (1988); in *Weak Interactions and Neutrinos*, Proceedings of the Twelfth International Workshop, Ginosar, Israel, 1989, edited by P. Singer and B. Gad Eilam [Nucl. Phys. B (Proc. Suppl.) **13**, 527 (1990)].

[38] T. K. Kuo and J. Pantaleone, Rev. Mod. Phys. **61**, 937 (1989).

[39] D. C. Kennedy, in *Testing the Standard Model*, Proceedings of the 1990 Theoretical Advanced Study Institute in Elementary Particle Physics, Boulder, 1990, edited by M. Cvetič and P. Langacker (World Scientific, Singapore, 1991), p. 807.

[40] P. B. Pal, Int. J. Mod. Phys. A **7**, 5387 (1992).

[41] K. S. Hirata *et al.*, Phys. Rev. Lett. **66**, 9 (1991).

[42] R. Sienkiewicz, J. N. Bahcall, and B. Paczyński, Astrophys. J. **349**, 641 (1988).

[43] I. J. Sackmann, A. I. Boothroyd, and W. A. Fowler, Astrophys. J. **360**, 727 (1990).

[44] P. Langacker, University of Pennsylvania Report No., UPR 0401T, 1989 (unpublished); R. Barbieri and A. Dolgov, Nucl. Phys. B **349**, 743 (1991); K. Enqvist, K. Kainulainen, and J. Maalampi, Phys. Lett. B **249**, 531 (1990); M. J. Thomson and B. H. J. McKellar, *ibid.* **259**, 113 (1991); V. Barger *et al.*, Phys. Rev. D **43**, 1759 (1991); P. Langacker and J. Liu, *ibid.* **46**, 4140 (1992).

[45] X. Shi, D. Schramm, and B. Fields, Phys. Rev. D **48**, 2563 (1993).

[46] D. Dearborn (private communications).

[47] A similar prediction was given previously by J. N. Bahcall and H. A. Bethe, Phys. Rev. Lett. **65**, 2233 (1990); A. J. Baltz and J. Weneser, Phys. Rev. D **66**, 520 (1991). We consider it worthwhile to update the prediction by using the latest Homestake and Kamiokande results and including the theoretical uncertainties.

[48] G. T. Ewan *et al.* "Sudbury Neutrino Observatory Proposal," Report No. SNO-87-12, 1987 (unpublished); "Scientific and Technical Description of the Mark II SNO Detector," edited by E. W. Beier and D. Sinclair, Report No. SNO-89-15, 1989 (unpublished).

[49] Y. Totsuka, University of Tokyo (ICRR) Report No. ICCR-Report-227-90-20, 1990 (unpublished).

[50] "BOREXINO at Gran Sasso — proposal for a real time detector for low energy solar neutrinos," Vol. 1, edited by G. Bellini, M. Campanella, D. Giugni, and R. Raghavan (1991).

[51] C. Rubbia, Report No. CERN-PPE/93-08, 1993 (unpublished).

[52] S. Nozawa, private communications.

[53] M. Doi and K. Kubodera, Phys. Rev. C **45**, 1988 (1992); S. Ying, W. Haxton, and E. Henley, *ibid.* **45**, 1982 (1992); K. Kubodera and S. Nozawa, University of South Carolina Report No. USC(NT)-93-6 (unpublished) and references therein.

[54] J. M. LoSecco [31].

[55] See, for example, E. Beier *et al.*, Phys. Lett. B **283**, 446 (1992), and references therein.

[56] G. Smoot *et al.*, *ibid.* **396**, L1 (1992); E.L. Wright *et al.*, Astrophys. J. **396**, L13 (1992); R. Schaefer and Q. Shafi, Bartol Research Institute Report No. BA-93-52; Nature (London) **359**, 199 (1992); A. Klypin, J. Holtzman, J. Primack, and E. Regos, University of California (Santa Cruz) Report No. SCIPP-92-52 (unpublished); R. L. Davis *et al.*, Phys. Rev. Lett. **69**, 1856 (1992).

[57] P. Langacker, in *Proceedings of the 4th International Symposium on Neutrino Telescopes*, Venice, Italy, 1992, Boulder, 1990, edited by M. Bald-Ceolin (University of Padua, Padua, 1992), p. 73.

[58] M. Cvetič and P. Langacker, Phys. Rev. D **46**, R2759 (1992).

[59] G. Bernardi, in *Proceedings of the XXIV International Conference on High Energy Physics*, Munich, West Germany, 1988, edited by R. Kotthaus and J. Kühn (Springer, Berlin, 1989), p. 1076.

FIG. 10. The combined allowed regions are simply taken as overlaps of the three experimental constraints at 95% C.L. This C.L. definition overestimates the uncertainties, allowing a parameter space which is marginally allowed by different experiments, but, in fact, its χ^2 is large and the combined fit is poor. As a result the obtained parameter space is significantly overestimated compared to Fig. 5, especially in the large-angle region; even a third allowed region appears in large-angle, small Δm^2. Also this overlap procedure ignores uncertainty correlations between different experiments.

FIG. 11. The allowed regions of the combined experiments using different C.L definitions; (a) the Monte Carlo SSMs, (b) the Monte Carlo SSMs using the overlap of the experimental and theoretical uncertainties [20,21]. The latter method overestimates the allowed regions.

FIG. 12. The allowed regions of the combined experiments using an improved C.L definition that assumes a Gaussian probability density for each solution. The 90, 95, and 99 % C.L. correspond to (a) $\Delta\chi^2 = 5.9$, 7.3, and 10.6, ignoring the Earth effect and (b) $\Delta\chi^2 = 5.5$, 7.0, and 10.9, including the Earth effect.

FIG. 13. The updated result of the combined MSW analysis assuming the Bahcall-Pinsonneault SSM. The Earth effect, Kamiokande II day-night data, theoretical uncertainties and their correlations of the parametrized method are included, and the improved C.L. definition is used.

FIG. 14. The updated result of the combined MSW analysis for the oscillations into sterile neutrinos. The Bahcall-Pinsonneault SSM is assumed. The Earth effect, Kamiokande II day-night data, theoretical uncertainties and their correlations of the parametrized method are included, and the improved C.L. definition is used.

FIG. 15. The combined allowed regions for oscillations into sterile neutrinos (a) without and (b) with the Earth effect. No solutions are allowed in the large-angle regions even at 99% C.L.

FIG. 16. The experimental constraints assuming nonstandard solar models that predict neutrino fluxes *smaller* than the SSM: (a) the opacity is reduced by 20% at temperature larger than 5×10^6 K [46], (b) S_{11} is increased by 30% [14].

FIG. 17. The experimental constraints assuming nonstandard solar models that predict neutrino fluxes *larger* than the SSM: (a) a high Y model [27,28] and (b) the maximum rate model in which S_{33} is artificially set to zero, maximizing the gallium rate to 303 SNU [8].

FIG. 18. The allowed regions of the combined observations when the central temperature (T_C) is a completely free parameter. The combined data constrain T_C to 1.02 ± 0.02 (1σ), which is consistent with the SSM ($T_C = 1 \pm 0.006$). Also displayed is the region excluded by the Kamiokande day-night data at 90% C.L.; the exclusion comes from the comparison between the different time bins, and is insensitive to the absolute ^{8}B flux or T_C.

FIG. 19. The experimental constraints when nonstandard S_{17} values are assumed. S_{17} is directly proportional to the ^{8}B flux and has the largest uncertainty among the SSM input parameters. We take S_{17} to be (a) 30% smaller than the SSM, (b) 50% larger than the SSM. In (c) the ^{8}B flux is treated as a completely free parameter; the combined data constraint ^{8}B $= 1.43 + 0.65 - 0.42$ of the standard value (1σ) with $\chi^2_{\min} = 2.0$ for 6 degrees of freedom. Also shown in (c) is the excluded region from the Kamiokande II day-night data (90% C.L.), which is independent of the ^{8}B flux magnitude.

FIG. 20. (a) The combined result of the Homestake and Kamiokande experiments. From the allowed regions we can predict the gallium rate to be $\leq$ 100 SNU at 95% C.L., which is consistent with the current observations of SAGE and GALLEX. (b) The combined result when the gallium experimental uncertainty is reduced by a factor $1/\sqrt{2}$, which is equivalent to the data set through the end of 1994. The central value of the gallium rate is assumed to stay at the current value. The present values are used for the other experiments.

FIG. 26. The contours of the signal to the SSM ratio including the time-averaged Earth effect for (a) the SNO charged current mode ($\nu_e + d \to p + p + e$), (b) Super-Kamiokande (νe scattering), and (c) BOREXINO (νe scattering). Superimposed are the combined current allowed regions at 95% C.L of the Homestake, Kamiokande, and gallium experiments.

FIG. 27. Shown are the constraints on the $\nu_e \leftrightarrow \nu_\mu$ and $\nu_\mu \leftrightarrow \nu_\tau$ oscillations [59], the constraints on the oscillations into sterile neutrinos ($\nu_e \leftrightarrow \nu_s$ and $\nu_\mu \leftrightarrow \nu_s$) from big-bang nucleosynthesis (BBN) [45], and three observational hints of neutrino mass: the MSW hypothesis for the solar neutrino deficit, the oscillation interpretation of the atmospheric neutrino deficit [55], and the cold plus hot dark matter scenario for the COBE and large scale structure data [56]. Also displayed are predictions from various theoretical models [11,57,58].

FIG. 4. The allowed regions of the Homestake, Kamiokande, and gallium experiments, and the combined observations. The Earth effect is not included. The SSM uncertainties are calculated by (a) the Bahcall-Ulrich 1000 Monte Carlo SSM's, (b) the parametrized Bahcall-Ulrich SSM, and (c) the parametrized Bahcall-Pinsonneault SSM. The comparison of (a) and (b) shows that the Monte Carlo method and our parametrization method are essentially equivalent. The allowed regions are defined by $\chi^2(\sin^2 2\theta, \Delta m^2) \leq \chi^2_{\min} + \Delta \chi^2$ with $\Delta \chi^2 = 6.0$ at 95% C.L.

FIG. 5. Same as Fig. 4, except that the Earth effect is included. The Kamiokande day-night data exclude the region shown with a dotted line (90% C.L.), and are incorporated in the combined fit.
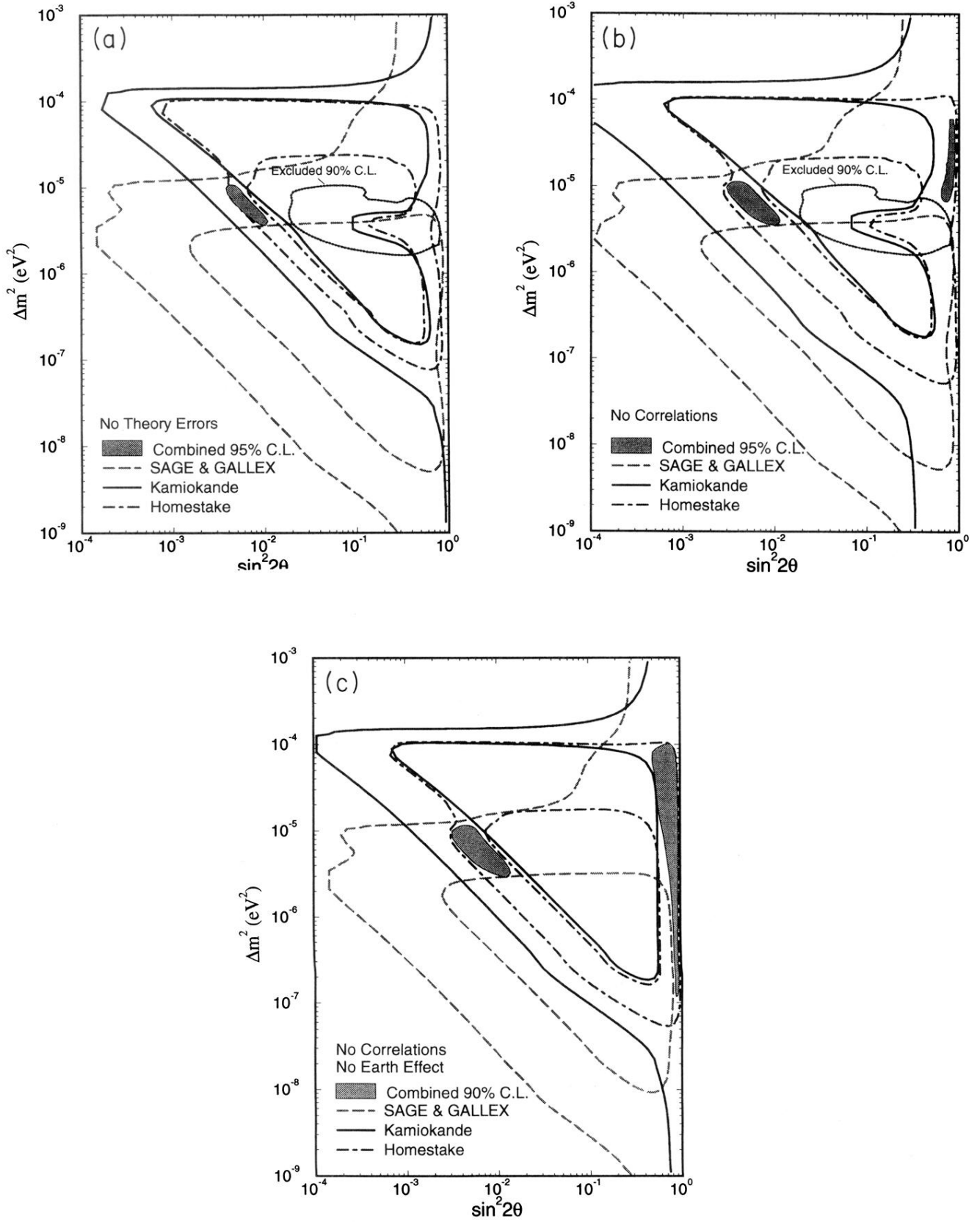
FIG. 6. The experimental constraints on the MSW parameters assuming the Bahcall-Pinsonneault SSM when (a) the theoretical uncertainties of the SSM fluxes and the detector cross sections are ignored, (b) the theoretical uncertainties are included, but their correlations between the fluxes and between the experiments are ignored. Displayed in (c) is the result at 90% C.L. calculated with the same condition in Ref. [24]: the correlations and the Earth effect are ignored and the same experimental input parameters are used. The omission of the correlations overestimates the allowed large-angle regions.
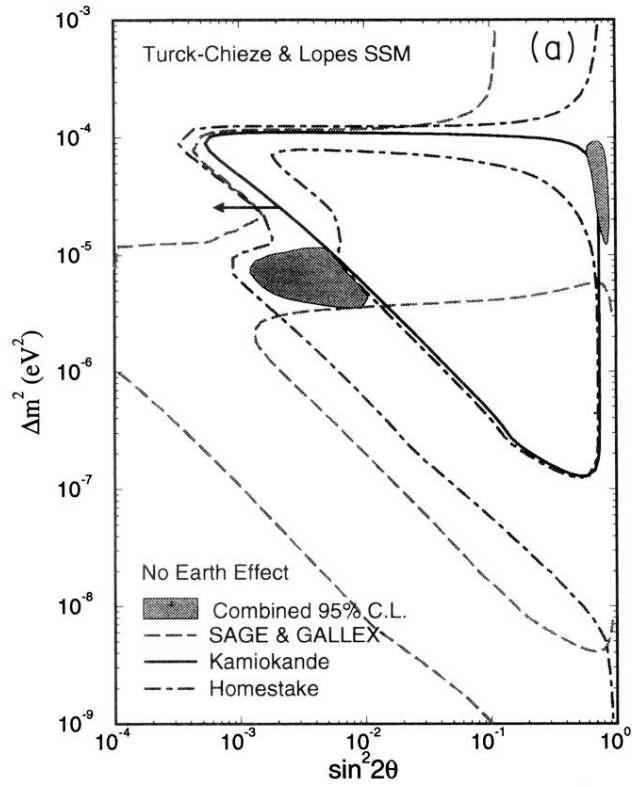
FIG. 7. The experimental constraints when the Turck-
Chièze–Lopes SSM is assumed. The two figures are (a) with-
out and (b) with the Earth effect. No constraints are obtained
at 95% C.L. from the upper limit of the the Kamiokande
result, and the Kamiokande allowed regions are outside the
triangles with the solid lines. The region excluded by the
Kamiokande II day-night data is shown with the dotted line
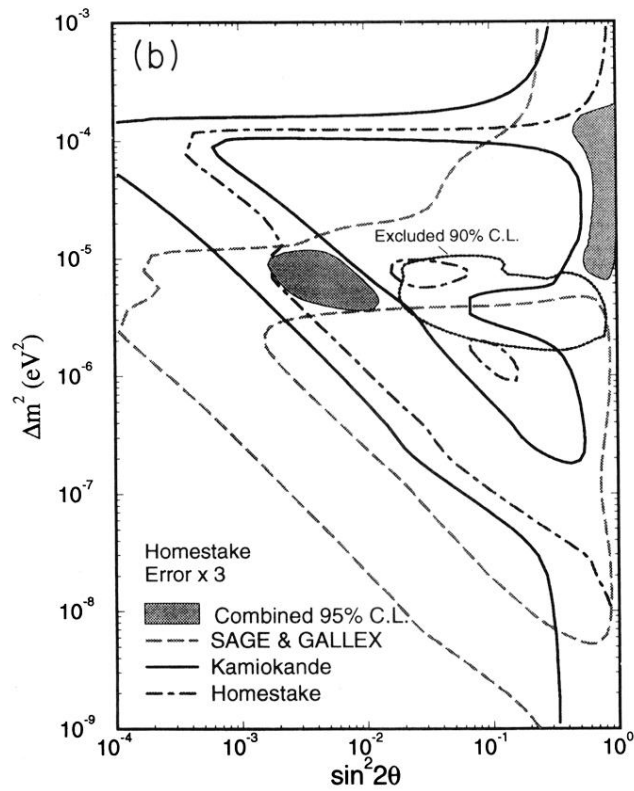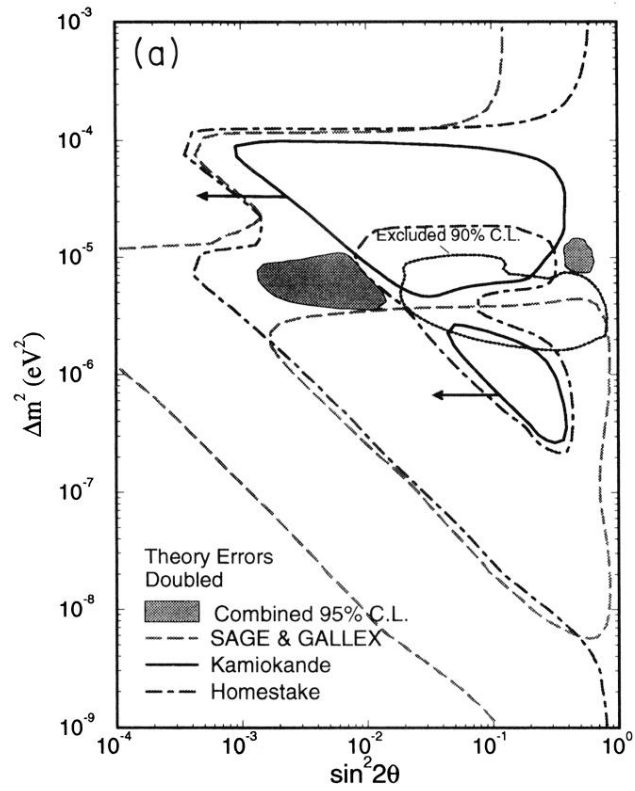(90% C.L.) in (b).

FIG. 8. The experimental constraints (a) when theoretical uncertainties of the Bahcall-Pinsonneault SSM fluxes and the detector cross sections are doubled and (b) the Homestake experimental uncertainty is tripled. The Earth effect and the Kamiokande II day-night data are included in both cases.
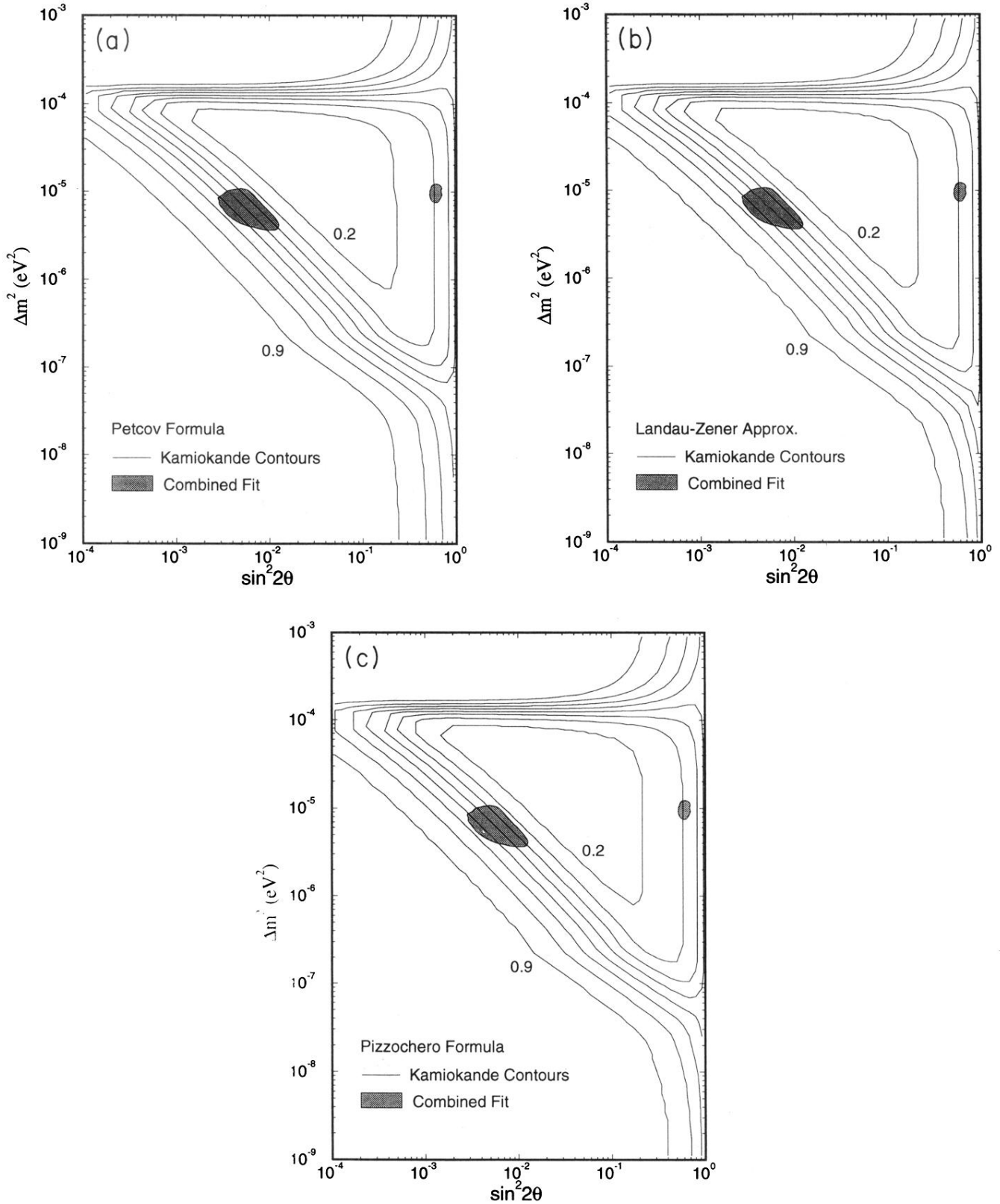
FIG. 9. The Kamiokande contours of the signal to SSM ratio (including the neutral current reaction in flavor oscillations) for three different analytic MSW approximations of (a) Petcov, (b) Parke, and (c) Pizzochero. The Earth effect is not included. The formulas by Parke and Pizzochero fail in the large-angle, small Δm^2 region ($\Delta m^2 \leq 3 \times 10^{-8} \text{eV}^2$). Also shown are the allowed regions of the combined observations including the Earth effect and the Kamiokande day-night data. We show the Kamiokande contours without the Earth effect since they involve only the ^{8}B flux and make a clean comparison possible. The energy resolution and the detector efficiency of Kamiokande are included.